

iKalibr: Unified Targetless Spatiotemporal Calibration for Resilient Integrated Inertial Systems

Shuolong Chen¹, Xingxing Li¹, Shengyu Li¹, Yuxuan Zhou¹, and Xiaoteng Yang¹

Abstract—The integrated inertial system, typically integrating an IMU and an exteroceptive sensor such as radar, LiDAR, and camera, has been widely accepted and applied in modern robotic applications for ego-motion estimation, motion control, or autonomous exploration. To improve system accuracy, robustness, and further usability, both multiple and various sensors are generally resiliently integrated, which benefits the system performance regarding failure tolerance, perception capability, and environment compatibility. For such systems, accurate and consistent spatiotemporal calibration is required to maintain a unique spatiotemporal framework for multi-sensor fusion. Considering most existing calibration methods (i) are generally oriented to specific integrated inertial systems, (ii) often only focus on spatial determination, (iii) usually require artificial targets, lacking convenience and usability, we propose *iKalibr*: a unified targetless spatiotemporal calibration framework for resilient integrated inertial systems, which overcomes the above issues, and enables both accurate and consistent calibration. Altogether four commonly employed sensors are supported in *iKalibr* currently, namely IMU, radar, LiDAR, and camera. The proposed method starts with a rigorous and efficient dynamic initialization, where all parameters in the estimator would be accurately recovered. Following that, several continuous-time-based batch optimizations would be carried out to refine initialized parameters to global optimal ones. Sufficient real-world experiments were conducted to verify the feasibility and evaluate the calibration performance of *iKalibr*. The results demonstrate that *iKalibr* can achieve accurate resilient spatiotemporal calibration. We open-source our implementations at (<https://github.com/Unsigned-Long/iKalibr>) to benefit the research community.

Index Terms—Spatiotemporal calibration, multi-sensor fusion, continuous-time batch optimization, resilient integration

I. INTRODUCTION

INTEGRATED inertial systems, such as visual-inertial [1]–[3], light detection and ranging (LiDAR)-inertial [4]–[6], and radar-inertial [7]–[9] systems, have been widely applied in a variety of robotic tasks, especially in accurate ego-motion estimation and autonomous exploration. To improve system performance in terms of failure tolerance, perception capability, and environment compatibility, multiple sensors, regarding both type [10]–[12] and quantity [13]–[15], are commonly integrated into the system, which has been affordable due to the significantly reduced price and power consumption of sensors in recent years. For such systems, accurate spatiotemporal

calibration is needed to determine unique spatial and temporal frameworks for multi-sensor fusion, as inaccurate spatiotemporal parameters would largely impair system performance.

Generally speaking, spatiotemporal calibration methods can be categorized as target-based and target-free ones, according to whether artificial targets are employed in calibration. In target-based methods, artificial targets, such as chessboards [16] and AprilTags [17] oriented to cameras, easy-to-identify geometries [18] oriented to LiDARs, or corner reflectors [19] oriented to radars, are introduced in calibration for efficient and accurate data association. Although precise calibration can be generally achieved in target-based methods, the requirement of additional artificial instruments largely limits their convenience and further usability. Differently, in target-free methods, natural targets rather than artificial ones, such as visual landmarks [20] or plane features [21], would be automatically extracted from environments to aid calibration, which significantly improves the usability, and supports on-site calibration. However, the calibration performance of existing target-free methods still holds a larger upgrade space compared with target-based ones.

Spatiotemporal calibration methods can also be categorized as online and offline ones. In online calibration, spatiotemporal parameters are estimated together with other interested states in real-time estimators, such as odometers [22], [23] or simultaneous localization and mapping (SLAMs) [24], where prior knowledge about initials of spatiotemporal parameters are generally required for system startup. Meanwhile, observability analysis and awareness of spatiotemporal parameters are required in online calibration [25], since the stable motion, expected by mapping-based estimators for continuous tracking, is not sufficiently excited and would lead to pretty weak spatiotemporal observability and further estimator rank deficit. In this sense, online calibration is more like a contradictory issue, even rigorous and meticulous observability-aware modules are involved in estimators (this would increase system complexity and is not conducive to both system stability and spatiotemporal convergence). Through sacrificing perfectionism but gaining considerable usability improvements, offline calibration organizes spatiotemporal determination as a decoupled problem, compared with online one. Although sufficiently excited motion is still required in offline calibration, especially for IMU-related calibration, motion excitation can be achieved conveniently without concerns.

To achieve optimal multi-sensor fusion, both spatial and temporal reference frameworks are required. Currently, most existing calibration methods [26]–[28] only focus on spatial determination (extrinsic determination), assuming sensors are

Manuscript received: xxxx; Revised: xxxx; Accepted: xxxx.

This work was supported by the National Key Research and Development Program of China under 2023YFB3907100. The authors are with the School of Geodesy and Geomatics (SGG), Wuhan University, Wuhan 430070, China. Corresponding author: Xingxing Li (xxli@sgg.whu.edu.cn).

The specific contributions of the authors to this work are listed in Section CRediT Authorship Contribution Statement at the end of the article.

Digital Object Identifier (DOI): see top of this page.

temporally hardware-synchronized. However, this could not hold for most low-cost smart devices, where only rough software-level time synchronization is conducted, leading to time offsets between sensors. In such cases, ignoring the temporal calibration would introduce inevitable errors in spatial determination. Considering this, most state-of-the-art methods [29]–[31] support both spatial and temporal determination in calibration, thus are capable of higher usability.

In terms of spatiotemporal estimation, continuous-time estimation, relying on continuous-time representation, has been deeply studied in recent years, and tends to be more popular than traditional discrete-time estimation. The continuous-time representation temporally decouples state estimates with sensor measurements, rather than tightly couples them by the discrete-time representation. Benefiting from this, continuous-time representation allows efficient state querying at arbitrary time instants by maintaining sparse but descriptive parameters [32], [33], which is more suitable for temporal calibration. Altogether two continuous-time representation methods are commonly utilized in the state estimation, namely nonparametric Gaussian processes (GPs) [34], [35] and parametric B-splines [29], [30]. Compared with GPs where additional motion priors are generally required to guarantee sparsity for computation acceleration, B-splines are born with sparsity due to the local controllability (determined by the prior spline order). Meanwhile, as piecewise polynomial functions, B-splines have closed-form expression, which allows efficient and accurate computation for analytical time derivatives.

Although numerous calibration methods oriented to specific minimum integrated inertial systems (integrate single IMU and single exteroceptive sensor) exist, varying from target-based to target-free, from online to offline, from spatial or temporal only to spatiotemporal, from discrete-time to continuous-time, multiple separate calibrations are generally required for more complex or resilient integrated inertial systems, which are labor-intensive and would lead to inconsistent spatiotemporal framework. In this article, focusing on resilient integrated inertial systems and taking into account both calibration accuracy and usability, we present a unified spatiotemporal calibration framework, termed *iKalibr*, which is targetless, offline, and continuous-time-based. *iKalibr* is capable of one-shot resilient spatiotemporal determination, and the key idea behind this is to adaptively maintain continuous-time kinematic curves in the estimator, such as rotation, linear acceleration, linear velocity, and translation curves, for different sensor suites, to guarantee maximum usability. This differs from traditional continuous-time-based methods, where a continuous-time trajectory is always maintained consistently. *iKalibr* starts with a rigorous initialization to recover initials of all states in estimator, followed by several batch optimizations, where initialized states would be iteratively and steadily refined to global optimal ones. *iKalibr* makes the following (potential) contributions:

- 1) As a continuous-time-based calibrator, *iKalibr* is capable of accurate, consistent, and compact spatiotemporal determination, requiring **no** additional artificial targets or facilities, prior knowledge, and aiding sensors (thus is a compact calibrator). Meanwhile, as a motion-based calibrator, *iKalibr* does **not** require overlapping fields of

iKalibr supports sensor suites that integrate

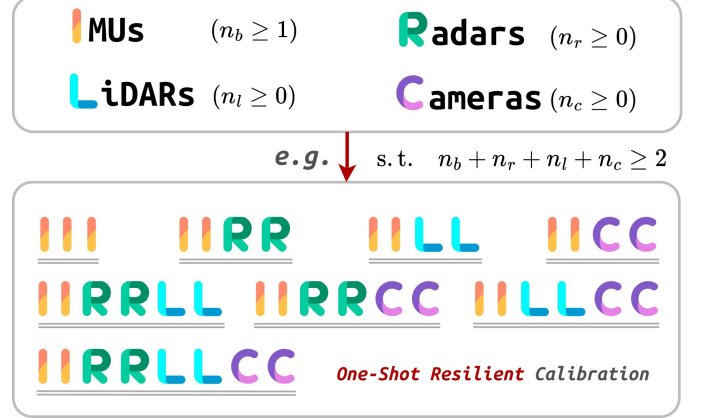


Fig. 1. Currently supported sensor suites in *iKalibr* for one-shot calibration.

view (FoVs) between sensors.

- 2) Due to the capability of **resilient** calibration, *iKalibr* supports numerous integrated inertial systems, and is capable of **one-shot** calibration, see Fig. 1. The IMUs, radars, LiDARs, and optical cameras are currently supported in *iKalibr*. Other types of sensors, such as the popular event cameras, can be easily extended in *iKalibr*.
- 3) A rigorous and efficient **dynamic** initialization procedure is designed in *iKalibr* to recover initial guesses of **all parameters** in the state vector from unknown states, which potentially benefits initialization of continuous-time-based real-time estimators, such as visual-inertial, LiDAR-inertial, radar-inertial odometers, or more complex integrated inertial systems, since both continuous-time curves and gravity vector would be accurately recovered alongside interested spatiotemporal parameters in initialization. Such an initialization would also benefit the online calibration methods by providing initials of spatiotemporal parameters for estimator startup.
- 4) Extensive real-world experiments are conducted to verify the feasibility and evaluate calibration performance of *iKalibr*, and the results demonstrate that *iKalibr* is capable of accurate, consistent, and resilient spatiotemporal calibration. Both the real-world datasets and code implementations are open-sourced, to benefit the robotic community if possible.

The rest of this article is structured as follows: Section II reviews the related spatiotemporal calibration works. Section III provides sensor models and continuous-time state representation. Section IV gives an overview of *iKalibr*. Section V and VI present the detailed calibration pipeline of initialization and batch optimization, respectively. Section VII reports the real-world experiments and results. Finally, Section VIII concludes our work and provides future directions.

II. RELATED WORKS

Related calibration works about sensors this work focuses on are extensive. Taking into account both readability and integrity, this section reviews the most relevant calibration works, organized according to sensor suite categories.

A. Visual-Inertial Calibration

It is no exaggeration to say that the visual-inertial suite is the most popular multi-sensor integration of the last decade. To determine the extrinsics of a visual-inertial suite, Mirzaei *et al.* [36] presented an extended Kalman filter (EKF)-based and chessboard-aided spatial calibrator, where a detailed observability analysis is also conducted. Similarly employing EKF but orienting to temporal calibration, Li *et al.* [22] proposed a visual-inertial system, supporting time offset determination. Focusing on both spatial and temporal calibration, Furgale *et al.* [29] presented the distinguished target-based *Kalibr*, which first introduces B-spline-based continuous-time estimation to calibration. *Kalibr* is then extended by Huai *et al.* [31] to support rolling shutter (RS) cameras. Different from global shutter (GS) cameras exposing an entire image simultaneously, the RS cameras expose consecutive rows of an image with a constant line delay, which requires calibration. Utilizing a non-parametric trajectory representation rather than the B-spline-based parametric one, Nikolic *et al.* [37] designed a spatiotemporal visual-inertial calibrator, where the inertial intrinsic determination is also considered. In addition to offline calibration, online calibration is also deeply studied. Yang *et al.* [20] proposed a graph-optimization-based visual-inertial navigation system, which supports online extrinsic calibration. More advancedly, Huai *et al.* [23] presented a visual-inertial odometer, which is capable of full calibration (extrinsic, temporal, and visual and inertial intrinsic). Meanwhile, both GS cameras and RS cameras are supported in [23]. Considering the weak observability of spatiotemporal parameters in online calibration, Yang *et al.* [25] performed an in-depth observability analysis for aided inertial navigation systems, where several degenerate motions are considered. More directly, Xiao *et al.* [38] designed a computationally efficient monitoring algorithm to explicitly determine when significant observability exists to support online visual-inertial recalibration.

B. LiDAR-Inertial Calibration

Compared with optical cameras, LiDARs almost suffer free from lighting conditions and can provide accurate and scale-aware dense point clouds. To calibrate extrinsics of LiDAR-inertial sensor suites, Liu *et al.* [18] introduced artificial cone and cylinder features as calibration targets to aid geometric constraint construction. Utilizing plane features extracted from structured environments, Le *et al.* [39] estimated LiDAR-inertial extrinsics based on a point-to-plane optimization framework. Similar to [39] but considering more geometric features in environments, Liu *et al.* [40] proposed a multi-feature on-site extrinsic calibration method for LiDAR-inertial systems. More weakly relying on structured environments, Mishra *et al.* [27] presented an EKF-based target-free extrinsic calibrator using the motion-based calibration constraint. To determine both spatial and temporal parameters, Lv *et al.* [30] proposed a target-free continuous-time-based spatiotemporal calibration method, i.e., the well-known *LI-Calib*, which performs spatiotemporal optimization based on IMU-derived kinematic constraints and LiDAR-derived point-to-plane constraints. In their further work, i.e., *OA-Calib*

[21], an observability-aware module is designed for accurate observability-constrained spatiotemporal determination. Similarly, as a continuous-time-based method but modeled by non-parametric GP, a targetless extrinsic calibration framework is proposed by Li *et al.* [41]. However, a priori dense point cloud map is required for plane feature extraction, thus potential inconvenience exists in application. Differently, focusing on online calibration, Wu *et al.* [42] recently presented an adaptive frame length odometry with robust LiDAR-inertial extrinsic estimation, where IMU-derived pre-integration constraints and LiDAR-derived point-to-plane constraints are introduced in optimization.

C. Radar-Related Calibration

Different from LiDARs, radars provide sparse target clouds and additional radial velocities utilizing lower-frequency measuring signals, thus considered as weather-robust sensors. Due to the shortage of radar-inertial calibration works, other radar-related works, such as radar-visual and radar-LiDAR, will also be discussed alongside radar-inertial ones in this section. To calibrate a 2D-radar-LiDAR suite, Peršić *et al.* [43] designed a triangular calibration target with a trihedral reflector for correspondence registration, and presented a radar cross section (RCS)-based two-stage optimization method for extrinsic determination. Focusing on 2D-radar-camera suites, Natour *et al.* [44] proposed a radar-visual extrinsic calibration method, where painted canonical targets are employed for radar-visual data association. To further jointly calibrate 2D-radar-camera-LiDAR suites, Domhof *et al.* [28] designed a calibration target consisting of four round holes and a trihedral corner reflector, which supports efficient data association among multi-model sensor measurements. Recently, 3D radars have become available and popular in robotic applications, which can provide additional elevation information of targets compared with 2D radars. Wise *et al.* [45] presented a continuous-time-based target-free 3D-radar-visual extrinsic calibrator, utilizing visual landmarks and radar-derived velocities. More advancedly, Doer *et al.* [46] proposed an EKF-based 3D-radar-inertial odometer, supporting online extrinsic calibration. However, initial guesses of extrinsics are required in this method.

D. Inertial-Inertial (Multi-IMU) Calibration

In practice, multi-IMU calibration could be solved through multiple separate sensor-IMU calibrations by introducing an additional aiding sensor, such as a camera, LiDAR, or radar. However, this could introduce potential inconsistency, and is labor-intensive. Considering the limitations, the authors of *Kalibr* extended it to support single-camera-aided multi-IMU extrinsic calibration in [47], where the visual chessboards are required. Similarly, Li *et al.* [48] extended the *LI-Calib* to support multi-LiDAR multi-IMU spatiotemporal calibration method, which could be considered as a LiDAR-aided multi-IMU calibrator. Differently, focusing on online multi-IMU calibration, Hartzer *et al.* [49] proposed an EKF-based visual-inertial odometer, supporting extrinsic determination. To ensure maximum usability, Lee *et al.* [50] presented an IMU-only dual-IMU extrinsic calibration method, which requires no additional aiding sensors compared with the above ones.

III. PRELIMINARIES

This section presents mathematical notations and coordinate frame definitions used throughout this article, corresponding sensor models and B-spline-based continuous-time representation for time-varying states are also described in detail.

A. Notations and Definitions

Altogether four commonly employed sensor types, namely IMU, radar, LiDAR, and optical camera, are considered in this work for resilient spatiotemporal calibration. Given an inertial system resiliently integrating a total of n_b IMUs, n_r radars, n_l LiDARs, and n_c cameras with

$$\begin{aligned} 1 \leq n_b \in \mathbb{N}, \quad 0 \leq n_r, n_l, n_c \in \mathbb{N}, \\ n_b + n_r + n_l + n_c \geq 2, \end{aligned} \quad (1)$$

we use $\underline{\mathcal{F}}_{b^i}$, $\underline{\mathcal{F}}_{r^j}$, $\underline{\mathcal{F}}_{l^k}$, and $\underline{\mathcal{F}}_{c^m}$ to denote the coordinate frames of the i -th IMU, j -th radar, k -th LiDAR, and m -th camera, respectively. We represent the six-degrees-of-freedom (DoF) rigid transform from $\underline{\mathcal{F}}_a$ to $\underline{\mathcal{F}}_b$ utilizing the Euclidean matrix \mathbf{T}_a^b in Lie group $\text{SE}(3)$, which is defined as follows:

$$\mathbf{T}_a^b \triangleq \begin{bmatrix} \mathbf{R}_a^b & \mathbf{p}_a^b \\ \mathbf{0}_{1 \times 3} & 1 \end{bmatrix} \quad (2)$$

where \mathbf{R}_a^b and \mathbf{p}_a^b denotes the rotation matrix in Lie group $\text{SO}(3)$ and translation vector in vector space \mathbb{R}^3 , respectively. In terms of their high-order kinematics, we use $\boldsymbol{\omega}_a^b \in \mathbb{R}^3$ and $\boldsymbol{\alpha}_a^b \in \mathbb{R}^3$ to express the angular velocity and acceleration of $\underline{\mathcal{F}}_a$ with respect to and parameterized in $\underline{\mathcal{F}}_b$. Similarly, $\mathbf{v}_a^b \in \mathbb{R}^3$ and $\mathbf{a}_a^b \in \mathbb{R}^3$ denotes the corresponding linear velocity and acceleration, respectively. τ_a^b denotes time offset from $\underline{\mathcal{F}}_a$ to $\underline{\mathcal{F}}_b$, i.e., $\tau_b = \tau_a + \tau_a^b$. The gravity vector is expressed as $\mathbf{g} \in \mathbb{R}^3$, which is considered as a two DoF quantity with a constant Euclidean norm. Finally, the noisy measurements and quantity estimates are denoted as $\tilde{(\cdot)}$ and $\hat{(\cdot)}$, respectively.

B. Sensor Models

1) *IMU Intrinsic Model*: As a proprioceptive sensor, IMU perceives the kinematics of the body in inertial space, providing high-frequency body-frame angular velocity and specific force measurements. Due to the potential inaccurate assembly and nominal scaling factors, and variable biases in output signals, IMU typically provides biased and noisy inertial measurements, especially the low-cost micro-electro-mechanical system (MEMS) IMUs. Adhering to [51], the inertial measurements from the IMU are modeled as

$$\begin{aligned} \tilde{\mathbf{a}} &= h_a(\mathbf{a}, \mathbf{x}_{\text{in}}^b) \triangleq \mathbf{M}_a \cdot \mathbf{a} + \mathbf{b}_a + \boldsymbol{\epsilon}_a \\ \tilde{\boldsymbol{\omega}} &= h_\omega(\boldsymbol{\omega}, \mathbf{x}_{\text{in}}^b) \triangleq \mathbf{M}_\omega \cdot \mathbf{R}_a^\omega \cdot \boldsymbol{\omega} + \mathbf{b}_\omega + \boldsymbol{\epsilon}_\omega \end{aligned} \quad (3)$$

where \mathbf{a} and $\boldsymbol{\omega}$ are ideal specific force and angular velocity in scaled orthogonal frame $\underline{\mathcal{F}}_b$, while $\tilde{\mathbf{a}}$ and $\tilde{\boldsymbol{\omega}}$ are noisy ones in update-to-scale non-orthogonal frames, see Fig. 2; $\underline{\mathcal{F}}_a$ and $\underline{\mathcal{F}}_\omega$ denote frames of the accelerometer and gyroscope respectively, which may not be coincident. In this work, only the rotational misalignment in inconsistency is considered, which is parameterized as \mathbf{R}_a^ω by assuming that $\underline{\mathcal{F}}_b$ coincides with $\underline{\mathcal{F}}_a$, i.e., $\underline{\mathcal{F}}_b \triangleq \underline{\mathcal{F}}_a$. \mathbf{M}_a and \mathbf{M}_ω are upper triangular

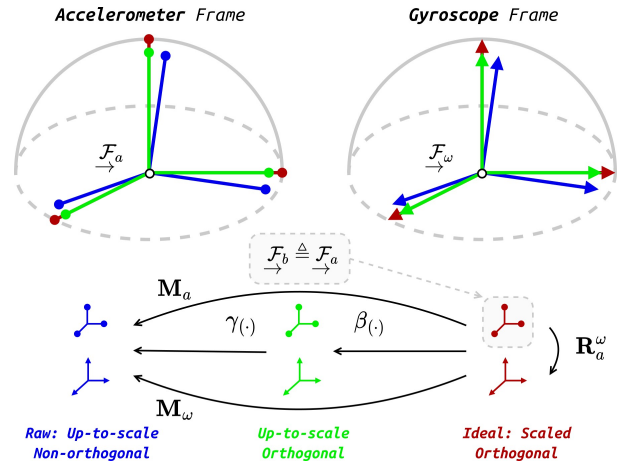


Fig. 2. Illustration of inertial measuring coordinates frames in an IMU. The rotational misalignment between accelerometer and gyroscope frames, non-orthogonality, and scale factors are considered here.

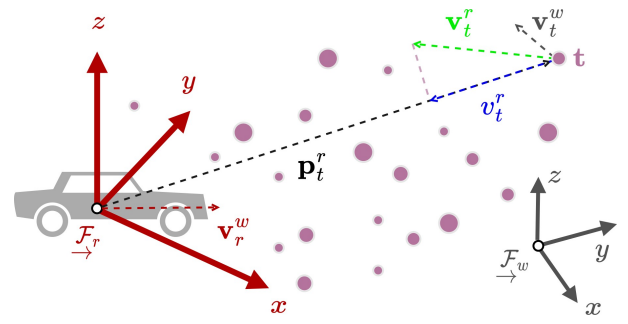


Fig. 3. Illustration of radar target measurements. Target position \mathbf{p}_t^r and its radial Doppler velocity v_t^r can be obtained when tracked by the radar.

mapping matrices, which introduce the scale factors $\beta_{(\cdot)}$ and non-orthogonality factors $\gamma_{(\cdot)}$ to associate the ideal frames with up-to-scale non-orthogonal ones:

$$\mathbf{M}_a \triangleq \begin{bmatrix} \beta_{a,1} & \gamma_{a,1} & \gamma_{a,2} \\ 0 & \beta_{a,2} & \gamma_{a,3} \\ 0 & 0 & \beta_{a,3} \end{bmatrix}, \quad \mathbf{M}_\omega \triangleq \begin{bmatrix} \beta_{\omega,1} & \gamma_{\omega,1} & \gamma_{\omega,2} \\ 0 & \beta_{\omega,2} & \gamma_{\omega,3} \\ 0 & 0 & \beta_{\omega,3} \end{bmatrix}. \quad (4)$$

\mathbf{b}_a and \mathbf{b}_ω denote time-varying biases of the accelerometer and gyroscope respectively, and can be considered as constants in a short period, which holds in the proposed calibration framework. The above intrinsic parameters, denoted as \mathbf{x}_{in}^b , can be pre-calibrated (see Appendix A), or jointly optimized with other parameters in spatiotemporal calibration if strong observability exists. $\boldsymbol{\epsilon}_a$ and $\boldsymbol{\epsilon}_\omega$ are corresponding zero-mean Gaussian white noises of sensors.

2) *Radar Doppler Velocity Model*: As an active exteroceptive sensor, radar measures the target position \mathbf{p}_t^r and its radial velocity v_t^r in $\underline{\mathcal{F}}_r$, i.e., the radial projection of the linear velocity of the target \mathbf{t} with respect to $\underline{\mathcal{F}}_r$ (see Fig. 3), which can be expressed as

$$\tilde{v}_t^r \triangleq \frac{(\tilde{\mathbf{p}}_t^r)^\top \cdot \mathbf{v}_t^r}{\|\tilde{\mathbf{p}}_t^r\|} + \epsilon_r = \frac{(\tilde{\mathbf{p}}_t^r)^\top \cdot (\mathbf{R}_r^w)^\top \cdot (\mathbf{v}_t^w - \mathbf{v}_r^w)}{\|\tilde{\mathbf{p}}_t^r\|} + \epsilon_r \quad (5)$$

with

$$\mathbf{v}_t^r = [\mathbf{p}_t^r]_\times \cdot (\mathbf{R}_r^w)^\top \cdot \boldsymbol{\omega}_r^w + (\mathbf{R}_r^w)^\top \cdot (\mathbf{v}_t^w - \mathbf{v}_r^w) \quad (6)$$

where \mathcal{F}_w denotes the world frame; $\|\cdot\|$ and $[\cdot]_\times$ represent the Euclidean norm and cross-product operation, respectively; ϵ_r denotes the measuring noise. When the target \mathbf{t} is stationary in \mathcal{F}_w , i.e., $\mathbf{v}_t^w \equiv \mathbf{0}_{3 \times 1}$, (5) can be rewritten as

$$\tilde{\mathbf{v}}_t^r \triangleq -\frac{(\tilde{\mathbf{p}}_t^r)^\top \cdot (\mathbf{R}_r^w)^\top \cdot \mathbf{v}_r^w}{\|\tilde{\mathbf{p}}_t^r\|} + \epsilon_r, \quad (7)$$

which is assumed in the proposed spatiotemporal calibration for better usability and is generally easy to satisfy.

3) *Camera Model*: Working as an exteroceptive but passive sensor, the optical camera captures scenarios in the FoV and projects them onto the image plane, providing informative images. Optical images are generally distorted due to the deviation from rectilinear projection led by the manufacturing and assembly of the lens. While multiple visual projection and distortion models exist, the commonly employed pinhole [52] projection model, and Brown [53] and fish-eye [54] distortion models are considered in this work, which could be described as

$$\tilde{\mathbf{f}}_l^c = \begin{bmatrix} \tilde{u} \\ \tilde{v} \end{bmatrix} = \pi(\mathbf{p}_l^c, \mathbf{x}_{in}^c) + \epsilon_c \quad (8)$$

with

$$\pi(\mathbf{p}_l^c, \mathbf{x}_{in}^c) \triangleq \begin{bmatrix} f_x & 0 & c_x \\ 0 & f_y & c_y \end{bmatrix} \cdot \begin{bmatrix} d_x(x_n, y_n) \\ d_y(x_n, y_n) \\ 1 \end{bmatrix} \quad (9)$$

and

$$x_n = \frac{\mathbf{p}_{l,x}^c}{\mathbf{p}_{l,z}^c}, \quad y_n = \frac{\mathbf{p}_{l,y}^c}{\mathbf{p}_{l,z}^c} \quad (10)$$

where \mathbf{p}_l^c denotes the landmark position in \mathcal{F}_c , imaged as $\tilde{\mathbf{f}}_l^c$ on the image plane; \mathbf{x}_{in}^c is the camera intrinsics, which contains principle point (c_x, c_y) , focal length (f_x, f_y) , and distortion coefficients, and could be pre-calibrated conveniently using target-based intrinsic calibration method [16]; $\pi(\cdot)$ represents the pinhole projection function; $d_x(\cdot)$ and $d_y(\cdot)$ are Brown or fish-eye distortion functions in the x -axis and y -axis directions, respectively; ϵ_c denotes the imaging noise.

In addition to imaging models, the visual geometric imaging process also varies depending on the exposure mode, which can be categorized as GS and RS mechanisms. Consider that a landmark \mathbf{p}_l^w in \mathcal{F}_w is imaged as feature $\tilde{\mathbf{f}}_l^{c_i}$ in the i -th image frame, for the GS camera, such process could be described as

$$\tilde{\mathbf{f}}_l^{c_i} = \pi(\mathbf{p}_l^{c_i}, \mathbf{x}_{in}^c) + \epsilon_{c_i} \quad (11)$$

with

$$\mathbf{p}_l^{c_i} = \mathbf{R}_w^{c_i} \cdot \mathbf{p}_l^w + \mathbf{p}_w^{c_i}. \quad (12)$$

However, for the RS camera, which exposes consecutive rows of an image with a constant line delay τ_{ld} rather than exposing the entire image simultaneously like the GS camera, (11) should be rewritten as

$$\tilde{\mathbf{f}}_l^{c_i} = \pi(\mathbf{p}_l^{c_{i,v}}, \mathbf{x}_{in}^c) + \epsilon_{i,v} \quad (13)$$

with

$$\mathbf{p}_l^{c_{i,v}} = \mathbf{R}_{c_i}^{c_{i,v}} \cdot \mathbf{p}_l^{c_i} + \mathbf{p}_{c_i}^{c_{i,v}}, \quad \mathbf{p}_l^{c_i} = \mathbf{R}_w^{c_i} \cdot \mathbf{p}_l^w + \mathbf{p}_w^{c_i} \quad (14)$$

where $\mathcal{F}_{c_{i,v}}$ denotes the camera frame when exposing the v -th row of the i -th image, which is generally not coincident with \mathcal{F}_{c_i} in dynamic scenarios due to the RS exposure mechanism,

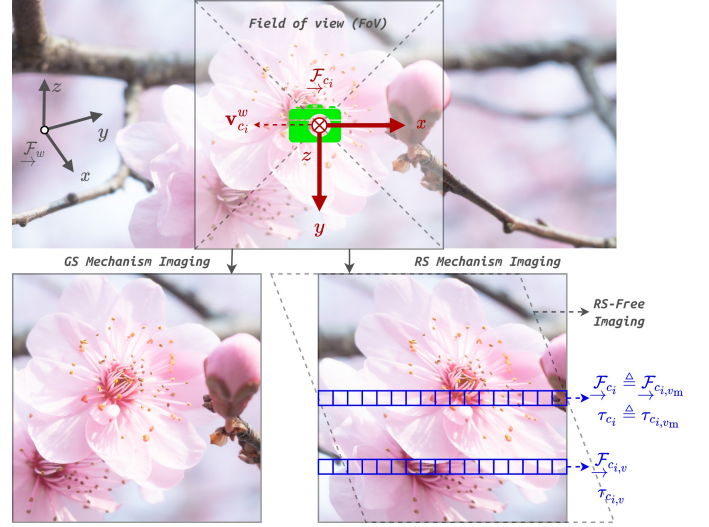


Fig. 4. Illustration of GS and RS mechanisms. All rows in an image are associated with a unique camera frame for GS mechanism, which does not hold for RS mechanism since rows are exposed sequentially in a readout timepiece. When relative motion exists between the RS camera and the scenario (movement to the left in this example), RS exposure mechanism leads to RS effect.

see Fig. 4. By assuming that \mathcal{F}_{c_i} coincides with the camera frame when exposing the **middle** row, i.e., $\mathcal{F}_{c_i} \triangleq \mathcal{F}_{c_{i,v_m}}$, we have

$$\tau_{c_{i,v}} = \tau_{c_i} + \left(\frac{v}{h} - \frac{1}{2} \right) \times \tau_{red} \quad (15)$$

where $\tau_{c_{i,v}}$ and $\tau_{c_i} \triangleq \tau_{c_{i,v_m}}$ denote the exposure time associated with $\mathcal{F}_{c_{i,v}}$ and \mathcal{F}_{c_i} , respectively; h denotes the image height of the camera; $\tau_{red} = h \times \tau_{ld}$ is the readout time of a RS image frame, which would be calibrated simultaneously with other spatiotemporal parameters in the proposed method. Note that (13) is a more general geometric imaging process description, equally applicable for GS camera by considering $\tau_{red} \equiv 0$, i.e., rows in a GS image frame are associated with a unique camera frame. In addition, although this work focuses on the optical camera, it's suitable for more advanced cameras, such as the RGB-D camera and the bio-inspired event camera, since optical images are generally provided simultaneously by these cameras.

C. Continuous-Time State Representation

To efficiently fuse the high-frequency and asynchronous multi-sensor measurements in calibration, the B-splines-based continuous-time representation is employed in this work to encode time-varying states in the estimator. Specifically, as an inertial-related spatiotemporal calibration framework, dynamic data acquisition is required, resulting in time-varying (i) rotational kinematics, associated with rotation-related spatiotemporal parameters such as extrinsic rotations, and (ii) translational kinematics, associated with linear-scale-related ones such as monocular visual scales and extrinsic translations. In this work, the rotation B-spline living in $SO(3)$ is employed for rotational kinematic representation. In terms of the linear scale B-spline living in \mathbb{R}^3 for translational kinematic representation, it varies adaptively (it can be translation,

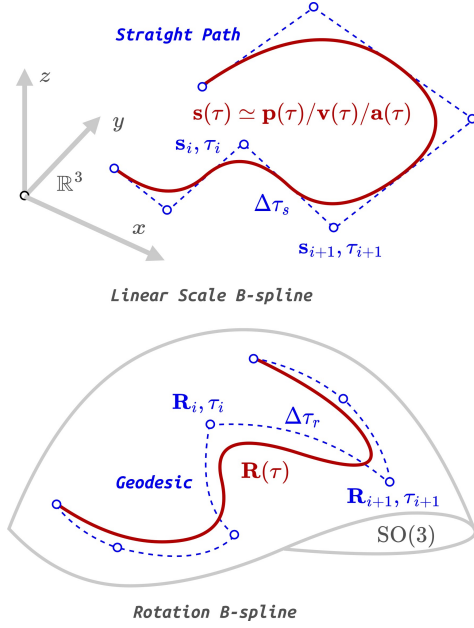


Fig. 5. Illustration of the linear scale B-spline living in \mathbb{R}^3 and the rotation B-spline living in $\text{SO}(3)$, where red curves represent B-splines, blue circles are control points connected by dashed lines. Different from the vector space where the distance between control points is measured by a straight line, the manifold of $\text{SO}(3)$ measures distance by geodesic (also known as great arc).

linear velocity, or linear acceleration) based on the involved resilient integrated inertial sensor suites in calibration to ensure usability and flexibility, see Fig. 5 and Fig. 6.

Specifically, given a series of linear scale control points (also known as knots, they could be translation, linear velocity, or acceleration ones) that are temporally uniformly distributed:

$$\mathcal{S} \triangleq \{\mathbf{s}_i, \tau_i \mid \mathbf{s}_i \in \mathbb{R}^3, \tau_i \in \mathbb{R}, i \in \mathbb{N}\} \quad (16)$$

s.t. $\tau_{i+1} - \tau_i \equiv \Delta\tau_s, \mathbf{s}_i \simeq \mathbf{p}_i/\mathbf{v}_i/\mathbf{a}_i,$

the linear scale quantity $\mathbf{s}(\tau)$ at time $\tau \in [\tau_i, \tau_{i+1})$ in a k -order uniform B-spline can be obtained by involving finite k control points:

$$\mathbf{s}(\tau) = \mathbf{s}_i + \sum_{j=1}^{k-1} \lambda_j(u) \cdot (\mathbf{s}_{i+j} - \mathbf{s}_{i+j-1}) \quad (17)$$

where $u = (\tau - \tau_i)/\Delta\tau_s$, and $\lambda_j(u)$ is the j -th element of vector $\boldsymbol{\lambda}(u)$ which is obtained from the order-determined cumulative matrix $\mathbf{N}^{(k)}$ and normalized time vector \mathbf{u} [32]:

$$\boldsymbol{\lambda}(u) = \mathbf{N}^{(k)} \cdot \mathbf{u} \quad \text{s.t.} \quad \mathbf{u} \triangleq [u^0 \quad u^1 \quad \dots \quad u^{k-1}]^\top. \quad (18)$$

In this work, the cubic ($k = 4$) B-spline is employed, which stays \mathcal{C}^2 continuous and thus ensures continuity of zero-order, first-order, and second-order kinematics, such as continuous translation, velocity, and acceleration if a translational B-spline is utilized. In such case, the cumulative matrix $\mathbf{N}^{(4)}$ could be expressed as

$$\mathbf{N}^{(4)} \triangleq \frac{1}{6} \begin{bmatrix} 6 & 0 & 0 & 0 \\ 5 & 3 & -3 & 1 \\ 1 & 3 & 3 & -2 \\ 0 & 0 & 0 & 1 \end{bmatrix}. \quad (19)$$

As for the rotation B-spline, due to the non-closedness of scalar multiplication on the manifold of $\text{SO}(3)$, the rotational

control points should be first mapped to the tangent space of $\text{SO}(3)$, i.e., the vector space of Lie algebra $\mathfrak{so}(3)$, for scaling, see Fig. 5. Specifically, given a series of rotational control points that are temporally uniformly distributed:

$$\mathcal{R} \triangleq \{\mathbf{R}_i, \tau_i \mid \mathbf{R}_i \in \text{SO}(3), \tau_i \in \mathbb{R}, i \in \mathbb{N}\} \quad (20)$$

s.t. $\tau_{i+1} - \tau_i \equiv \Delta\tau_r$

the rotation $\mathbf{R}(\tau)$ at time $\tau \in [\tau_i, \tau_{i+1})$ in a k -order uniform rotation B-spline can be obtained by involving finite k control points:

$$\mathbf{R}(\tau) = \mathbf{R}_i \cdot \prod_{j=1}^{k-1} \text{Exp} \left(\lambda_j(u) \cdot \text{Log} \left(\mathbf{R}_{i+j-1}^\top \cdot \mathbf{R}_{i+j} \right) \right) \quad (21)$$

where the capitalized exponential mapping function $\text{Exp}(\cdot)$ maps elements in the vector space of $\mathfrak{so}(3)$ to the manifold of $\text{SO}(3)$, while the capitalized logarithmic mapping function $\text{Log}(\cdot)$ is its inverse one. Note that the time distances of linear scale and rotation B-splines, i.e., $\Delta\tau_s$ and $\Delta\tau_r$, as hyperparameters determining the number of control points and further representation capability of B-splines, are generally not the same, which should be carefully considered in practice based on the measurement frequency of sensors and intensity of motion excitation to ensure both high-accuracy state representation and low-computation consumption.

IV. OVERVIEW

The structure of the proposed target-free spatiotemporal calibration method for resilient integrated inertial systems is shown in Fig. 6. Given the raw measurements from integrated sensors that undergo sufficiently excited motion, the dynamic initialization procedure is first performed, which sequentially recovers initial guesses of the rotation B-spline, spatiotemporal parameters of involved sensors alongside the world-frame gravity vector, and the linear scale B-spline, see Section V. The recovered linear scale B-spline type varies depending on the integrated sensor type, which can be linear acceleration B-spline, linear velocity B-spline, or translation B-spline, to guarantee both the usability and accuracy of the linear scale B-spline in calibration. After the initialization, data association is carried out to construct LiDAR point-to-surfel and visual reprojection correspondences, if corresponding sensors are involved in calibration, see Section VI-A. As for IMU and radar, no data association is required as the raw measurements can be tightly coupled in the continuous-time-based estimator. Finally, a continuous-time-based nonlinear graph optimization is conducted to refine all initialized states to global optimal ones, see Section VI-B. Note that the final batch optimization would be performed several times until the final convergence, where the spatiotemporal parameters are grouped and involved in the optimization sequentially rather than simultaneously for better convergence performance, see Section VI-C. To guarantee the consistency of the estimated spatiotemporal framework, an IMU is selected as the reference IMU (any one of multiple IMUs, its frame is denoted as \mathcal{F}_{br} in this article), whose kinematics coincide with the ones of maintained rotation and linear scale B-splines. Note that the spatiotemporal parameters of the reference IMU are set as identities and keep constant in optimization to ensure a unique least-squares solution.

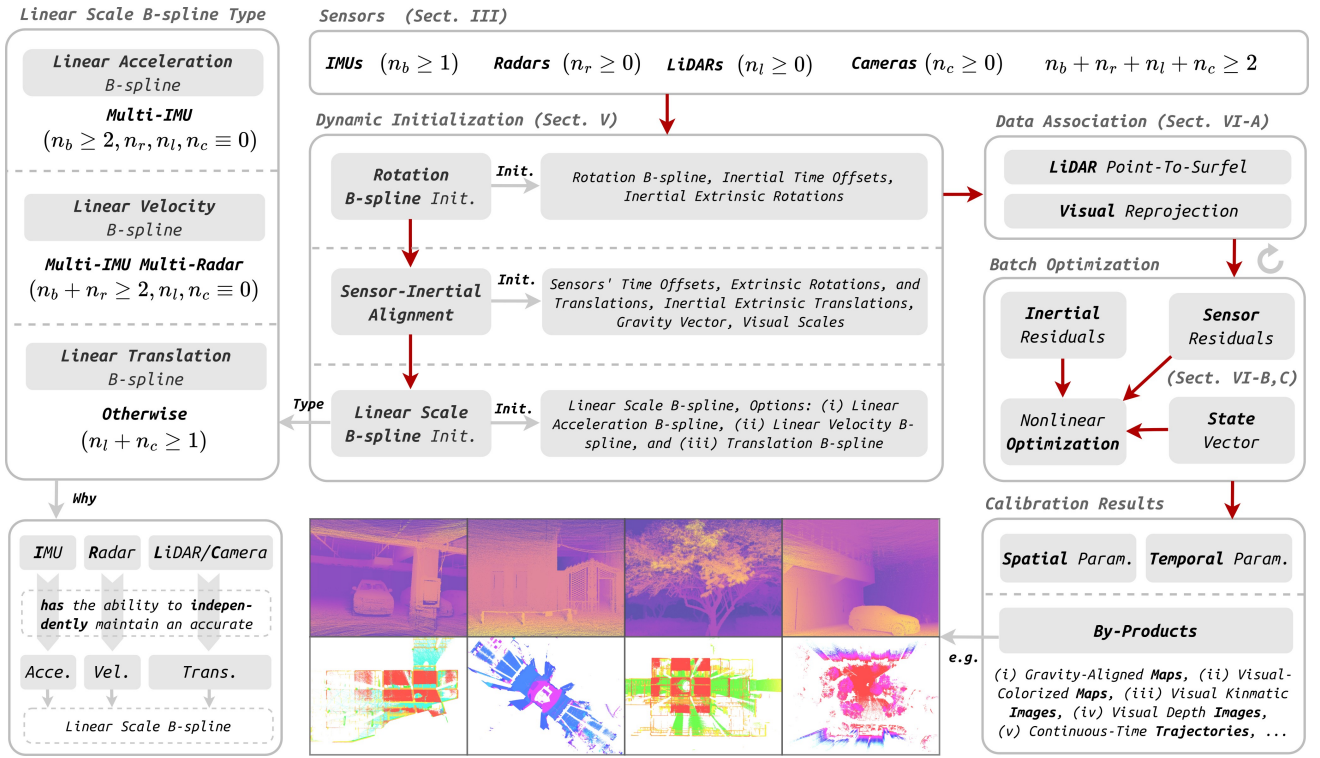


Fig. 6. Illustration of the full pipeline of the proposed targetless spatiotemporal calibration. The system starts with a dynamic initialization procedure, where initial guesses of spatiotemporal parameters and B-splines are recovered (see Section V). Subsequently, data association is performed to construct LiDAR point-to-surfel and visual reprojection correspondences if required (see Section VI-A). Finally, a global nonlinear continuous-time-based batch optimization (see Section VI-B) is carried out to iteratively refine (see Section VI-C) all initial states to global optimal ones. Though only four commonly employed sensor types, i.e., IMU, radar, LiDAR, and camera, are considered in this work currently, other types of sensors can be introduced conveniently.

The total state vector in the estimator contains spatiotemporal parameters, gravity vector, and control points of B-splines, which are expressed as follows:

$$\mathcal{X} \triangleq \{\mathbf{x}_{\text{rot}}, \mathbf{x}_{\text{pos}}, \mathbf{x}_{\text{tm}}, \mathbf{g}^w, \mathcal{S}, \mathcal{R}\} \quad (22)$$

with

$$\mathbf{x}_{(\cdot)} \triangleq \{\mathbf{x}_{(\cdot)}^b, \mathbf{x}_{(\cdot)}^r, \mathbf{x}_{(\cdot)}^l, \mathbf{x}_{(\cdot)}^c\} \text{ s.t. } (\cdot) \simeq \text{rot/pos/tm} \quad (23)$$

and

$$\begin{aligned} \mathbf{x}_{\text{rot}}^b &\triangleq \{\mathbf{R}_{b^i}^{b^r}\} & \mathbf{x}_{\text{pos}}^b &\triangleq \{\mathbf{p}_{b^i}^{b^r}\} & \mathbf{x}_{\text{tm}}^b &\triangleq \{\tau_{b^i}^{b^r}\} \\ \mathbf{x}_{\text{rot}}^r &\triangleq \{\mathbf{R}_{r^j}^{b^r}\} & \mathbf{x}_{\text{pos}}^r &\triangleq \{\mathbf{p}_{r^j}^{b^r}\} & \mathbf{x}_{\text{tm}}^r &\triangleq \{\tau_{r^j}^{b^r}\} \\ \mathbf{x}_{\text{rot}}^l &\triangleq \{\mathbf{R}_{l^k}^{b^r}\} & \mathbf{x}_{\text{pos}}^l &\triangleq \{\mathbf{p}_{l^k}^{b^r}\} & \mathbf{x}_{\text{tm}}^l &\triangleq \{\tau_{l^k}^{b^r}\} \\ \mathbf{x}_{\text{rot}}^c &\triangleq \{\mathbf{R}_{c^m}^{b^r}\} & \mathbf{x}_{\text{pos}}^c &\triangleq \{\mathbf{p}_{c^m}^{b^r}\} & \mathbf{x}_{\text{tm}}^c &\triangleq \{\tau_{c^m}^{b^r}, \tau_{\text{red}}^{c^m}\} \end{aligned} \quad (24)$$

$$\text{s.t. } 0 \leq i < n_b, \quad 0 \leq j < n_r, \quad 0 \leq k < n_l, \\ 0 \leq m < n_c, \quad i, j, k, m \in \mathbb{N}$$

where \mathbf{x}_{rot} , \mathbf{x}_{pos} , and \mathbf{x}_{tm} denote extrinsic rotations, extrinsic translations, and temporal parameters respectively, all of them are parameterized with respect to the reference IMU \mathcal{F}_{b^r} . Particularly, for RS camera, an additional temporal parameter, i.e., the readout time $\tau_{\text{red}}^{c^m}$, is considered in calibration. Note that the gravity vector and all control points in \mathcal{S} and \mathcal{R} are parameterized in \mathcal{F}_w , which is defined as the first frame of the reference IMU, i.e., $\mathcal{F}_w \triangleq \mathcal{F}_{b_0^r}$.

V. DYNAMIC INITIALIZATION

As a highly nonlinear system, the continuous-time tightly-coupled state estimator requires reasonable and accurate initial guesses of involved parameters for a global optimal solution and better convergence performance in the final batch optimization. Considering this, a rigorous and efficient multi-stage initialization procedure is carried out, which sequentially recovers the rotation B-splines, the spatiotemporal parameters with the gravity vector, and the linear scale B-spline. To avoid introducing unnecessary stationary prior and be consistent with the requirement of dynamic data acquisition, the initialization is performed dynamically (mainly on gravity determination), which significantly enhances both usability and flexibility.

A. Rotation B-spline Recovery

Given the raw body-frame angular velocity measurements from multiple gyroscopes ($n_b \geq 1$), the rotation B-spline could be first recovered, alongside additional inertial extrinsic rotations and time offsets if $n_b > 1$, which is achieved by solving the following nonlinear least-squares problem:

$$\{\hat{\mathbf{R}}, \hat{\mathbf{x}}_{\text{rot}}^b, \hat{\mathbf{x}}_{\text{tm}}^b\} = \arg \min \sum_i \sum_n^{\mathcal{D}_\omega^i} \|r_\omega(\tilde{\omega}_n^i)\|_{\mathbf{Q}_{\omega, n}^i}^2 \quad (25)$$

with

$$\begin{aligned} r_\omega(\tilde{\omega}_n^i) &\triangleq h_\omega(\omega^i(\tau_n + \hat{\tau}_{b^i}^{b^r}), \mathbf{x}_{\text{in}}^{b^i}) - \tilde{\omega}_n^i \\ \omega^i(\tau) &= (\mathbf{R}_{b^r}^w(\tau) \cdot \hat{\mathbf{R}}_{b^i}^{b^r})^\top \cdot \omega_{b^r}^w(\tau) \end{aligned} \quad (26)$$

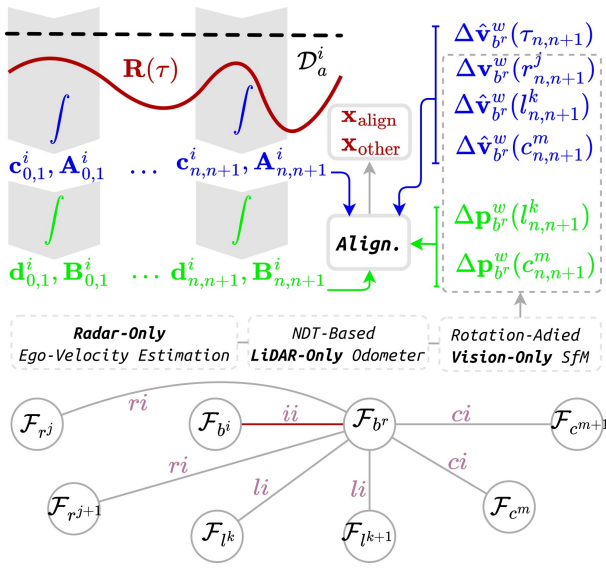


Fig. 7. Illustration of the sensor-inertial alignment. Sensor-inertial alignment constraints can be constructed between inertial sensors and other ones based on the initialized rotation B-spline $\mathbf{R}(\tau)$, inertial specific force measurements \mathcal{D}_a^i , and sensor-derived kinematics. ii , ri , li , and ci denote the constraints from inertial-inertial, radar-inertial, LiDAR-inertial, and visual-inertial alignments, respectively.

where \mathcal{D}_ω^i denotes the noisy angular velocity data sequence from the i -th gyroscope, in which $\tilde{\omega}_n^i$ is the n -th measurement at time τ_n stamped by \mathcal{F}_{b^i} ; $r_\omega(\cdot)$ is the gyroscope residual with information matrix $\mathbf{Q}_{\omega,n}^i$ determined by measurement noise level; $\mathbf{R}_{br}^w(\tau)$ and $\omega_{br}^w(\tau)$ are the ideal rotation and angular velocity at time τ , analytically obtained from the rotation B-spline based on (21), which exactly involves the rotation control points into the optimization.

B. Sensor-Inertial Alignment

Based on the fitted rotation B-spline and recovered inertial extrinsic rotation and time offsets, the uninitialized spatiotemporal parameters and world-frame gravity vector can be determined by aligning the inertial measurements with sensor-derived kinematics, namely IMU-derived linear accelerations, radar-derived linear velocities, and LiDAR-derived and visual-derived poses, see Fig. 7. Note that the alignment constraints described in the following subsections would be introduced resiliently (independently) into a unique least-squared problem for one-shot alignment. More mathematical details about alignment constraints can be found in Appendix B.

1) *Inertial-Inertial Alignment*: When multiple IMUs ($n_b > 1$) are involved in calibration, inertial-inertial alignment constraints would be constructed between \mathcal{F}_{b^i} and \mathcal{F}_{b^r} , which introduces the estimation of the inertial extrinsic translations and world-frame gravity vector.

Specifically, consider a timepiece $[\tau_n, \tau_{n+1})$, the linear velocity variation of \mathcal{F}_{b^r} can be expressed as:

$$\mathbf{v}_{b^r}^w(\tau_{n+1}) - \mathbf{v}_{b^r}^w(\tau_n) = \mathbf{c}_{n,n+1}^i - \mathbf{A}_{n,n+1}^i \cdot \mathbf{p}_{b^i}^{b^r} + \mathbf{g}^w \cdot \Delta\tau_{n,n+1} \quad (27)$$

with

$$\begin{aligned} \mathbf{c}_{n,n+1}^i &\triangleq \int_{\tau_n}^{\tau_{n+1}} \mathbf{R}_{b^r}^w(t) \cdot \mathbf{R}_{b^i}^{b^r} \cdot \mathbf{a}^i(s) \cdot dt, \quad s = t - \tau_{b^i}^{b^r} \\ \mathbf{A}_{n,n+1}^i &\triangleq \int_{\tau_n}^{\tau_{n+1}} \left([\alpha_{b^r}^w(t)]_\times + [\omega_{b^r}^w(t)]_\times^2 \right) \cdot \mathbf{R}_{b^r}^w(t) \cdot dt \end{aligned} \quad (28)$$

where integration terms $\mathbf{c}_{n,n+1}^i$ and $\mathbf{A}_{n,n+1}^i$ can be obtained numerically based on the recovered rotation B-spline, inertial extrinsic rotations, and time offsets by (25); s and t in integration are times stamped by \mathcal{F}_{b^i} and \mathcal{F}_{b^r} , respectively. By stacking multiple timepieces, the inertial-inertial alignment constraints would be introduced based on (27), where world-frame linear velocities, i.e., $\mathbf{v}_{b^r}^w(\cdot)$, are treated as estimates alongside other interested quantities in the problem.

2) *Radar-Inertial Alignment*: When multiple radars ($n_r > 0$) are involved in calibration, radar-inertial alignment constraints would be constructed between \mathcal{F}_{r^j} and \mathcal{F}_{b^r} , which introduces the estimation of radar extrinsics (both rotations and translations) and world-frame gravity vector. The radar-inertial alignment constraint in timepiece $[\tau_n, \tau_{n+1})$ is similar to the one in (27). The difference is that the world-frame linear velocities of \mathcal{F}_{b^r} , i.e., $\mathbf{v}_{b^r}^w(\cdot)$, are derived by the radar, rather than treated as estimates in inertial-inertial alignment.

Specifically, consider the k -th scan $\mathcal{S}_r^j(\tau_k)$ from the j -th radar, which wraps multiple targets measurements, the radar-frame linear velocity of the j -th radar at time τ_k , i.e., $\mathbf{v}_{\tau_k}^{r^j} \triangleq (\mathbf{R}_{r^j}^w(\tau_k))^T \cdot \mathbf{v}_{r^j}^w(\tau_k)$, is estimated first based on (7) as follows:

$$\hat{\mathbf{v}}_{\tau_k}^{r^j} = \arg \min \sum_n^{S_r^j(\tau_k)} \left\| \left(\tilde{\mathbf{p}}_{k,n}^{r^j} \right)^T \cdot \hat{\mathbf{v}}_{\tau_k}^{r^j} + \tilde{v}_{k,n}^{r^j} \cdot \|\tilde{\mathbf{p}}_{k,n}^{r^j}\| \right\|_{\mathbf{Q}_{r,k}^j}^2 \quad (29)$$

where $(\tilde{\mathbf{p}}_{k,n}^{r^j}, \tilde{v}_{k,n}^{r^j}) \in \mathcal{S}_r^j(\tau_k)$ are position and radial velocity of the n -th target in k -th scan of the j -th radar. The random sample consensus (RANSAC)-based outlier rejection is employed in problem (29) to reject model-inconsistent dynamic targets. Based on the estimated radar-frame linear velocity, the world-frame linear velocity of \mathcal{F}_{b^r} can be expressed as:

$$\mathbf{v}_{b^r}^w(\tau_k^j) \triangleq \mathbf{v}_{b^r}^w(\tau) = \mathbf{R}_{b^r}^w(\tau) \cdot \mathbf{R}_{r^j}^{b^r} \cdot \mathbf{v}_{\tau_k}^{r^j} - [\omega_{b^r}^w(\tau)]_\times \cdot \mathbf{R}_{b^r}^w(\tau) \cdot \mathbf{p}_{r,j}^{b^r} \quad (30)$$

which involves the extrinsics of radars. (27) and (30) would be organized together as radar-inertial alignment constraints.

3) *LiDAR-Inertial Alignment*: When LiDARs ($n_l > 0$) are involved in calibration, LiDAR-inertial alignment constraints would be constructed between \mathcal{F}_{l^k} and \mathcal{F}_{b^r} , which introduces the estimation of LiDAR extrinsics and gravity vector.

The normal distributions transform (NDT)-based LiDAR-only odometer [55] is first performed for each LiDAR independently to obtain rough poses. Considering that the NDT algorithm relies on good initials when performing scan registration, we first (i) try to recover rough rotations using the non-prior NDT, then (ii) employ the rotation-only hand-eye alignment to recover the extrinsic rotation using the rough rotations of \mathcal{F}_{l^k} and the rotation B-spline of \mathcal{F}_{b^r} , and finally (iii) perform a rotation-aided NDT to obtain accurate LiDAR poses. Such a strategy is reasonable since sufficiently excited motion is required in calibration, and generally contradicts accurate scan registration using non-prior NDT (challenging).

Specifically, given a rotation sequence \mathcal{S}_l^k containing multiple NDT-derived rough rotations of the \mathcal{F}_{l^k} , the rotation-only hand-eye alignment can be performed by solving the following least-squares problem:

$$\{\hat{\mathbf{R}}_{l^k}^{b^r}, \hat{\tau}_{l^k}^{b^r}\} = \arg \min \sum_n \left\| \hat{\mathbf{R}}_{l^k}^{b^r} \cdot \mathbf{R}_{l_{n+1}^k}^{l_n^k} \left(\mathbf{R}_{b_{n+1}^r}^{b_n^r} \hat{\mathbf{R}}_{l^k}^{b^r} \right)^\top \right\|_{\mathbf{Q}_{l,n}^k}^2 \quad (31)$$

with

$$\begin{aligned} \mathbf{R}_{l_{n+1}^k}^{l_n^k} &\triangleq \left(\mathbf{R}_{l^k}^{m^k}(\tau_n) \right)^\top \cdot \mathbf{R}_{l^k}^{m^k}(\tau_{n+1}) \\ \mathbf{R}_{b_{n+1}^r}^{b_n^r} &\triangleq \left(\mathbf{R}_{b^r}^w(\tau_n + \hat{\tau}_{l^k}^{b^r}) \right)^\top \cdot \mathbf{R}_{b^r}^w(\tau_{n+1} + \hat{\tau}_{l^k}^{b^r}) \end{aligned} \quad (32)$$

where $\mathbf{R}_{l^k}^{m^k}(\tau_n) \in \mathcal{S}_l^k$ is the NDT-derived rotation of n -th scan, which is expressed in the map frame \mathcal{F}_{m^k} ; $\mathbf{R}_{b^r}^w(\cdot)$ is the rotation of the reference IMU obtained from the fitted rotation B-spline. Note that both extrinsic rotation and time offset can be roughly determined for each LiDAR based on (31).

To construct LiDAR-inertial alignment constraints, similarly to radar, the linear velocity of \mathcal{F}_{b^r} in (27) would be rewritten as:

$$\mathbf{v}_{b^r}^w(l_\tau^k) \triangleq \mathbf{v}_{b^r}^w(\tau) = \mathbf{v}_{l^k}^w(\tau) - [\boldsymbol{\omega}_{b^r}^w(\tau)]_\times \cdot \mathbf{R}_{b^r}^w(\tau) \cdot \mathbf{p}_{l^k}^{b^r} \quad (33)$$

which is similar to (30). The difference is that linear velocities of the LiDAR, i.e., $\mathbf{v}_{l^k}^w(\cdot)$, are treated as estimates here. By continuing to perform time integration on (27), NDT-derived positions can be involved in alignment constraints:

$$\begin{aligned} \mathbf{p}_{b^r}^w(\tau_{n+1}) - \mathbf{p}_{b^r}^w(\tau_n) &= \mathbf{d}_{n,n+1}^i - \mathbf{B}_{n,n+1}^i \cdot \mathbf{p}_{b^i}^{b^r} \\ &\quad + \mathbf{v}_{b^r}^w(\tau_n) \cdot \Delta\tau_{n,n+1} + \frac{1}{2} \cdot \mathbf{g}^w \cdot \Delta\tau_{n,n+1}^2 \end{aligned} \quad (34)$$

with

$$\begin{aligned} \mathbf{p}_{b^r}^w(l_\tau^k) &\triangleq \mathbf{p}_{b^r}^w(\tau) = \mathbf{R}_{m^k}^w \cdot \mathbf{p}_{l^k}^{m^k}(\tau) + \mathbf{p}_{m^k}^w - \mathbf{R}_{b^r}^w(\tau) \cdot \mathbf{p}_{l^k}^{b^r} \\ \mathbf{d}_{n,n+1}^i &\triangleq \int_{\tau_n}^{\tau_{n+1}} \mathbf{R}_{b^r}^w(t) \cdot \mathbf{R}_{b^i}^{b^r} \cdot \mathbf{a}^i(s) \cdot dt^2, \quad s = t - \tau_{b^i}^{b^r} \\ \mathbf{B}_{n,n+1}^i &\triangleq \int_{\tau_n}^{\tau_{n+1}} \left([\boldsymbol{\alpha}_{b^r}^w(t)]_\times + [\boldsymbol{\omega}_{b^r}^w(t)]_\times^2 \right) \cdot \mathbf{R}_{b^r}^w(t) \cdot dt^2 \end{aligned} \quad (35)$$

where $\mathbf{R}_{m^k}^w = \mathbf{R}_{b^r}^w(\tau_m^k + \tau_{l^k}^{b^r}) \cdot \mathbf{R}_{l^k}^{b^r}$ denotes the rotation bias between \mathcal{F}_{m^k} and \mathcal{F}_w , τ_m^k is the map time, which is usually set to the time of the first registered scan of NDT; $\mathbf{p}_{m^k}^w$ is the position bias, which keeps unknown but would be eliminated in (34) by subtraction; integration terms $\mathbf{d}_{n,n+1}^i$ and $\mathbf{B}_{n,n+1}^i$, similar to $\mathbf{c}_{n,n+1}^i$ and $\mathbf{A}_{n,n+1}^i$, can be obtained numerically. (27), (33), and (34) would be organized together as LiDAR-inertial alignment constraints.

4) *Visual-Inertial Alignment*: When cameras ($n_c > 0$) are involved in calibration, visual-inertial alignment constraints would be constructed between \mathcal{F}_{c^m} and \mathcal{F}_{b^r} , which introduces the estimation of visual extrinsics and gravity vector.

The structure from motion (SfM) is first performed for each monocular camera to recover visual structure, namely up-to-scale poses and landmarks. To accelerate feature matching and visual reconstruction in SfM, we first (i) conduct a rotation-only visual odometer to obtain rotation sequence, and similar to LiDAR, (ii) employ the rotation-only hand-eye alignment to recover the visual extrinsic rotation, finally (iii) perform a rotation-aided vision-only SfM. Specifically, in the

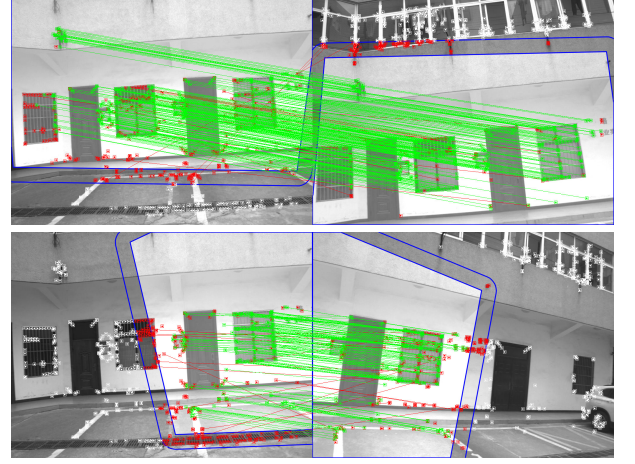


Fig. 8. Schematic of feature matching in the covisibility region found using the relative rotation by assuming a pure-rotation motion. White features are out-region ones and not involved in matching, red features are in-region (blue polygon) but matching-failed ones (outlier rejection using [57]), and green features are in-region and matched ones. Considering the existence of translation motion, an expanded buffer (blue rounded polygon) is constructed to relax the assumption of the pure-rotation motion.

rotation-only visual odometer, feature pairs of two consecutive frames tracked by KLT sparse optical flow algorithm [56] would be undistorted and involved in a frame-to-frame direct rotation optimization [57]. Different from pose recovery using fundamental or essential matrix models, the direct rotation optimization method decoupled the rotation estimation with translation, thus relative rotation can be solved accurately even for structural degeneracy or zero-translation motion. After rotations are recovered, a least-squares problem similar to (31) would be organized and solved to obtain extrinsic rotation and time offset. At this point, the accurate world-frame rotation of each image frame can be computed based on the rotation B-spline, extrinsic rotation, and time offset. In SfM, by assuming a pure-rotation motion, SIFT [58]-based feature matching between **arbitrary** two images is performed in the covisibility region (if it exists), which can be found by relative rotation based on priori world-frame rotations, see Fig. 8. The final incremental SfM would be performed in COLMAP [59].

Similar to LiDAR-inertial alignment, equations similar to (27), (33), and (34) would be organized together as visual-inertial alignment constraints. The difference is that SfM-derived visual poses are up-to-scale ones since monocular camera lacks observability for metric scale. By introducing explicit global visual scale, the position $\mathbf{p}_{b^r}^w(\tau)$ in (34) can be rewritten as:

$$\mathbf{p}_{b^r}^w(c_\tau^k) \triangleq \mathbf{p}_{b^r}^w(\tau) = \beta^k \cdot \mathbf{R}_{m^k}^w \cdot \mathbf{p}_{c^k}^{m^k}(\tau) + \mathbf{p}_{m^k}^w - \mathbf{R}_{b^r}^w(\tau) \cdot \mathbf{p}_{c^k}^{b^r} \quad (36)$$

where $\mathbf{p}_{c^k}^{m^k}(\tau)$ denotes the SfM-derived up-to-scale position at time τ ; β^k denotes the global scale of the visual structure, which would be estimated in alignment.

5) *One-Shot Sensor-Inertial Alignment Optimization*: Finally, the least-squares problem of the sensor-inertial align-

ment can be described as follows:

$$\begin{aligned} & \hat{\mathbf{x}}_{\text{align}} \cup \{\hat{\mathbf{v}}_{b^r}^w(\tau)\} \cup \{\hat{\mathbf{v}}_{l^k}^w(\tau)\} \cup \{\hat{\mathbf{v}}_{c^m}^w(\tau)\} \cup \{\hat{\beta}^m\} = \\ & \arg \min \sum_n \left(\sum_i^{n_b} \left\| r_v(b_n^i, b_{n+1}^i) \right\|^2 + \sum_j^{n_r} \left\| r_v(r_n^j, r_{n+1}^j) \right\|^2 \right. \\ & \quad + \sum_k^{n_l} \left\| r_v(l_n^k, l_{n+1}^k) \right\|^2 + \sum_m^{n_c} \left\| r_p(l_n^k, l_{n+1}^k) \right\|^2 \\ & \quad \left. + \sum_m^{n_c} \left\| r_v(c_n^m, c_{n+1}^m) \right\|^2 + \sum_m^{n_c} \left\| r_p(c_n^m, c_{n+1}^m) \right\|^2 \right) \end{aligned} \quad (37)$$

with

$$\begin{aligned} r_v(b_n^i, b_{n+1}^i) & \triangleq \hat{\mathbf{v}}_{b^r}^w(\tau_{n+1}) - \hat{\mathbf{v}}_{b^r}^w(\tau_n) - \Delta \mathbf{v}_{n,n+1}^{r,i} \\ r_v(r_n^j, r_{n+1}^j) & \triangleq \hat{\mathbf{v}}_{b^r}^w(r_{n+1}^j) - \hat{\mathbf{v}}_{b^r}^w(r_n^j) - \Delta \mathbf{v}_{n,n+1}^{r,j} \\ r_v(l_n^k, l_{n+1}^k) & \triangleq \hat{\mathbf{v}}_{b^r}^w(l_{n+1}^k) - \hat{\mathbf{v}}_{b^r}^w(l_n^k) - \Delta \mathbf{v}_{n,n+1}^{r,r} \\ r_p(l_n^k, l_{n+1}^k) & \triangleq \hat{\mathbf{p}}_{b^r}^w(l_{n+1}^k) - \hat{\mathbf{p}}_{b^r}^w(l_n^k) - \Delta \mathbf{p}_{n,n+1}^{r,r} \\ r_v(c_n^m, c_{n+1}^m) & \triangleq \hat{\mathbf{v}}_{b^r}^w(c_{n+1}^m) - \hat{\mathbf{v}}_{b^r}^w(c_n^m) - \Delta \mathbf{v}_{n,n+1}^{r,r} \\ r_p(c_n^m, c_{n+1}^m) & \triangleq \hat{\mathbf{p}}_{b^r}^w(c_{n+1}^m) - \hat{\mathbf{p}}_{b^r}^w(c_n^m) - \Delta \mathbf{p}_{n,n+1}^{r,r} \end{aligned} \quad (38)$$

and

$$\begin{aligned} \hat{\mathbf{x}}_{\text{align}} & \triangleq \hat{\mathbf{x}}_{\text{rot}} \cup \hat{\mathbf{x}}_{\text{pos}} \cup \hat{\mathbf{g}}^w \\ \Delta \mathbf{v}_{n,n+1}^{r,i} & \triangleq \tilde{\mathbf{c}}_{n,n+1}^i - \tilde{\mathbf{A}}_{n,n+1}^i \cdot \hat{\mathbf{p}}_{b^r}^{b^r} + \hat{\mathbf{g}}^w \cdot \Delta \tau_{n,n+1} \\ \Delta \mathbf{p}_{n,n+1}^{r,i} & \triangleq \tilde{\mathbf{d}}_{n,n+1}^i - \tilde{\mathbf{B}}_{n,n+1}^i \cdot \hat{\mathbf{p}}_{b^r}^{b^r} \\ & \quad + \mathbf{v}_{b^r}^w(l_n^k | c_n^m) \cdot \Delta \tau_{n,n+1} + \frac{1}{2} \cdot \hat{\mathbf{g}}^w \cdot \Delta^2 \tau_{n,n+1} \end{aligned} \quad (39)$$

where $\mathbf{v}_{b^r}^w(r_n^j)$ from (30), $\mathbf{v}_{b^r}^w(l_n^k | c_n^m)$ from (33), $\mathbf{p}_{b^r}^w(l_n^k)$ from (34), and $\mathbf{p}_{b^r}^w(c_n^m)$ from (36) are sensor-derived kinematics; $\Delta \mathbf{v}_{n,n+1}^{r,i}$ and $\Delta \mathbf{p}_{n,n+1}^{r,i}$ are velocity and position variations of \mathcal{F}_{b^r} in time piece $[\tau_n, \tau_{n+1})$, computed based on inertial measurements of \mathcal{F}_{b^i} ; \mathcal{S}_{tp} denotes time piece sequence. Note that the world-frame gravity vector should be solved on the sphere manifold to ensure a constant magnitude. After alignment optimization, the SfM-derived up-to-scale visual structures (landmarks and poses) would be scaled using the estimated global scale factors, if cameras are involved in calibration.

C. Linear Scale B-spline Recovery

Based on the initialized quantities from the previous two stages, the linear scale B-spline living in \mathbb{R}^3 would be recovered, whose type is resiliently selected from (i) linear acceleration B-spline, (ii) linear velocity B-spline, and (iii) linear translation B-spline, based on the sensor suite to be calibrated. Note that such resilient modeling aims to maximize calibration usability in terms of low computation complexity and high calibration accuracy.

1) *Linear Acceleration B-spline Recovery*: When only multiple IMUs are involved in spatiotemporal calibration, i.e.,

$$n_b \geq 2, n_r, n_l, n_c \equiv 0, \quad (40)$$

the linear acceleration B-spline would be treated as the linear scale B-spline, and recovered using raw specific force measurements from multiple accelerometers, which could be conducted by solving the following least-squares problem:

$$\hat{\mathcal{S}} = \arg \min \sum_i^{n_b} \sum_n^{\mathcal{D}_a^i} \left\| r_a(\tilde{\mathbf{a}}_n^i) \right\|_{\mathbf{Q}_{a,n}^i}^2 \quad (41)$$

with

$$\begin{aligned} r_a(\tilde{\mathbf{a}}_n^i) & \triangleq h_a(\mathbf{a}^i(\tau_n + \hat{\tau}_{b^i}^{b^r}), \mathbf{x}_{\text{in}}^{b^i}) - \tilde{\mathbf{a}}_n^i \\ \mathbf{a}^i(\tau) & = (\mathbf{R}_{b^r}^w(\tau) \cdot \hat{\mathbf{R}}_{b^i}^{b^r})^\top \cdot (\mathbf{a}_{b^i}^w(\tau) - \mathbf{g}^w) \\ \mathbf{a}_{b^i}^w(\tau) & = \mathbf{a}_{b^r}^w(\tau) + ([\boldsymbol{\alpha}_{b^r}^w(\tau)]_\times + [\boldsymbol{\omega}_{b^r}^w(\tau)]_\times^2) \cdot \mathbf{R}_{b^r}^w(\tau) \cdot \mathbf{p}_{b^i}^{b^r} \end{aligned} \quad (42)$$

where \mathcal{D}_a^i denotes the noisy specific force data sequence from the i -th accelerometer, in which $\tilde{\mathbf{a}}_n^i$ is the n -th measurement at time τ_n stamped by \mathcal{F}_{b^i} ; $r_a(\cdot)$ is the accelerometer residual with information matrix $\mathbf{Q}_{a,n}^i$; Similar as $\mathbf{R}_{b^r}^w(\tau)$, $\boldsymbol{\omega}_{b^r}^w(\tau)$, and $\boldsymbol{\alpha}_{b^r}^w(\tau)$, the linear acceleration $\mathbf{a}_{b^r}^w(\tau)$ could be analytically obtained from the linear scale B-spline based on (17), which exactly involves the linear scale control points into the optimization.

2) *Linear Velocity B-spline Recovery*: When additional radars are involved in spatiotemporal calibration, i.e.,

$$n_b + n_r \geq 2, n_l, n_c \equiv 0, \quad (43)$$

the linear velocity B-spline is treated as the linear scale B-spline, and recovered using raw target measurements from multiple radars and the specific force data from the reference IMU, which could be conducted by solving the following least-squares problem:

$$\begin{aligned} \{\hat{\mathcal{S}}, \hat{\mathbf{x}}_{\text{tm}}^r\} & = \arg \min \sum_j^{n_r} \sum_n^{\mathcal{D}_r^j} \left\| r_r(\tilde{\mathbf{p}}_n^{r,j}, \tilde{v}_n^{r,j}) \right\|_{\mathbf{Q}_{r,n}^j}^2 \\ & \quad + \sum_n^{\mathcal{D}_a^r} \|r_a(\tilde{\mathbf{a}}_n^r)\|_{\mathbf{Q}_{a,n}^r}^2 \end{aligned} \quad (44)$$

with

$$\begin{aligned} r_r(\tilde{\mathbf{p}}_n^{r,j}, \tilde{v}_n^{r,j}) & \triangleq \tilde{v}_n^{r,j} + \frac{(\tilde{\mathbf{p}}_n^{r,j})^\top (\mathbf{R}_{r,j}^w(t_n))^\top \cdot \mathbf{v}_{r,j}^w(t_n)}{\|\tilde{\mathbf{p}}_n^{r,j}\|} \\ \mathbf{R}_{r,j}^w(\tau) & = \mathbf{R}_{b^r}^w(\tau) \cdot \mathbf{R}_{b^j}^{b^r}, \quad t_n \triangleq \tau_n + \hat{\tau}_{r,j}^{b^r} \\ \mathbf{v}_{r,j}^w(\tau) & = \mathbf{v}_{b^r}^w(\tau) + [\boldsymbol{\omega}_{b^r}^w(\tau)]_\times \cdot \mathbf{R}_{b^r}^w(\tau) \cdot \mathbf{p}_{r,j}^{b^r} \end{aligned} \quad (45)$$

where \mathcal{D}_r^j is the noisy target measurements from the j -th radar; $r_r(\cdot)$ denotes the Doppler velocity residual with information matrix $\mathbf{Q}_{r,n}^j$. Note that the uninitialized time offsets of radars would be also recovered in this problem by introducing the accelerometer residual of the reference IMU, i.e., $r_a(\cdot)$.

3) *Linear Translation B-spline Recovery*: When LiDARs or cameras exist in spatiotemporal calibration, i.e.,

$$n_l + n_c \geq 1, \quad (46)$$

the linear translation B-spline would be treated as the linear scale B-spline and recovered using world-frame NDT-derived and scaled SfM-derived positions, which could be achieved by solving the following least-squares problem:

$$\begin{aligned} \hat{\mathcal{S}} & = \arg \min \sum_k^{n_l} \sum_n^{\mathcal{P}_{l^k}} \|r_p(\tilde{\mathbf{p}}_{l^k}^w(\tau_n))\|_{\mathbf{Q}_{l,n}^k}^2 \\ & \quad + \sum_m^{n_c} \sum_n^{\mathcal{P}_{c^m}} \|r_p(\tilde{\mathbf{p}}_{c^m}^w(\tau_n))\|_{\mathbf{Q}_{c,n}^m}^2 \end{aligned} \quad (47)$$

with

$$\begin{aligned} r_p(\tilde{\mathbf{p}}_{\text{sor}}^w(\tau_n)) & \triangleq \mathbf{R}_{b^r}^w(t_n) \cdot \mathbf{p}_{\text{sor}}^{b^r} + \mathbf{p}_{b^r}^w(t_n) - \tilde{\mathbf{p}}_{\text{sor}}^w(\tau_n) \\ t_n & \triangleq \tau_n + \tau_{\text{sor}}^{b^r}, \quad \mathcal{P}_{\text{sor}} \triangleq \{\tilde{\mathbf{p}}_{\text{sor}}^w(\tau_n)\}, \quad \text{sor} \simeq l^k/c^m \end{aligned} \quad (48)$$

TABLE I
RECOVERED STATES IN DYNAMIC INITIALIZATION

State	Meaning	Recovered In	LSQ Prob.
\mathcal{R}	knots of the rotation B-spline	Section V-A	(25)
$\mathbf{x}_{\text{rot}}^b$	extrinsic rotations of IMUs	Section V-A	(25)
\mathbf{x}_{tm}^b	time offsets of IMUs	Section V-A	(25)
$\mathbf{x}_{\text{rot}}^l$	extrinsic rotations of LiDARs	Section V-B	(31)
\mathbf{x}_{tm}^l	time offsets of LiDARs	Section V-B	(31)
$\mathbf{x}_{\text{rot}}^c$	extrinsic rotations of cameras	Section V-B	(31)
\mathbf{x}_{tm}^c	time offsets of cameras	Section V-B	(31)
$\mathbf{x}_{\text{pos}}^r$	extrinsic translations	Section V-B	(37)
$\mathbf{x}_{\text{rot}}^r$	extrinsic rotations of radars	Section V-B	(37)
\mathbf{g}^w	world-frame gravity vector	Section V-B	(37)
\mathcal{S}	knots of the scale B-spline	Section V-C	(41/44/47)
\mathbf{x}_{tm}^r	time offsets of radars	Section V-C	(44)

where \mathcal{P}_{l^k} and \mathcal{P}_{c^m} denote the position sequence of \mathcal{F}_{l^k} and \mathcal{F}_{c^m} , respectively. If additional radars are also involved in this case, their time offsets would be recovered subsequently by solving the least-squares problem described in (44), where linear scale control points would be fixed and not optimized. The only difference is that the linear velocities of the reference IMU, required in (44), would be obtained as the first-order kinematics of the linear translation B-spline here, rather than as the zero-order kinematics of linear velocity B-spline.

At this point, **all parameters** in the state vector have been initialized rigorously, which benefits the following continuous-time-based batch optimization significantly in terms of convergence performance and global optimal solution. For better readers' understanding of the total initialization process, we provide Table I to show when and where states are recovered.

VI. CONTINUOUS-TIME BATCH OPTIMIZATION

Based on results from the multi-stage initialization procedure, a continuous-time-based batch optimization graph would be constructed and solved iteratively to refine all initialized parameters to global optimal states. While raw measurements from IMUs and radars can be tightly coupled into the optimization, scans from LiDARs and images from cameras require data association to construct correspondences for optimization.

A. Data Association

Data association is first performed for LiDARs and cameras, where point-to-surfel and visual reprojection correspondences would be constructed based on NDT-derived rough LiDAR maps and SfM-derived visual structures, respectively.

1) *Point-to-Surfel Association for LiDARs*: Based on the recovered extrinsics and B-splines, the point cloud scans of multiple LiDARs would be first transformed to the world frame \mathcal{F}_w and merged as a unique global point cloud map. This global map is then organized as an octree-based multi-level voxel tree using UFOMap [60], where each voxel stores the mean vector, covariance matrix, and covariance-derived planarity of contained points.

Based on the voxel tree, we first transform each raw point in LiDAR scans expressed in \mathcal{F}_{l^k} to \mathcal{F}_w and then find all candidate voxels that (i) contain enough points (an

empirical threshold) when being constructed, (ii) contain this up-to-associated point, (iii) has depth between maximum and minimum depth thresholds, (iv) has planarity larger than the minimum planarity threshold, and (v) has point-to-surfel distance smaller than maximum distance threshold. If such voxels exist, we would continue to select a voxel with the largest planarity and construct a corresponding surfel to associate it with this point, as a point-to-surfel correspondence. To reduce computation complexity, all identified point-to-surfel correspondences would be downsampled, where each surfel is expected to associate a similar number of points. The final total point-to-surfel correspondences of the k -th LiDAR can be expressed as:

$$\mathcal{D}_l^k \triangleq \left\{ \tau_n, \tilde{\mathbf{p}}_n^k, \mathbf{e}_s^w \mid n \in \mathbb{N}, s \in \mathbb{N} \right\}, \quad \mathbf{e}_s^w \triangleq \begin{bmatrix} \mathbf{n}_s^w \\ d_s^w \end{bmatrix} \quad (49)$$

where $\tilde{\mathbf{p}}_n^k$ is the n -th raw LiDAR point stamped as τ_n and expressed in \mathcal{F}_{l^k} ; \mathbf{e}_s^w denotes the s -th world-frame surfel plane defined by normal vector $\mathbf{n}_s^w \in \mathbb{R}^3$ and distance $d_s^w \in \mathbb{R}$.

2) *Visual Reprojection Association for Cameras*: Based on the scaled SfM-derived visual landmarks, visual reprojection association is performed for each camera separately to construct visual reprojection correspondences.

Specifically, given a world-frame visual landmark captured by enough images (an empirical threshold), we first transform it to the camera coordinate frame that first captures it and then obtain its corresponding inverse depth in this image. The inverse depth together with the raw 2D image observation would be associated with other image observations of this landmark, as visual reprojection correspondences. Similar to point-to-surfel correspondences, the visual reprojection correspondences would be downsampled to reduce computation complexity. The final total visual reprojection correspondences of the m -th camera can be expressed as:

$$\mathcal{D}_c^m \triangleq \left\{ \tau_n, \tilde{\mathbf{f}}_l^{c_n^m}, \lambda_l^{c_n^m}, \tau_s, \tilde{\mathbf{f}}_l^{c_s^m} \mid n \in \mathbb{N}, s \in \mathbb{N} \right\} \quad (50)$$

where $\tilde{\mathbf{f}}_l^{c_n^m}$ is the first observation of the landmark captured by the n -th image stamped as τ_n , the corresponding inverse depth is denoted as $\lambda_l^{c_n^m}$; $\tilde{\mathbf{f}}_l^{c_s^m}$ is another observation captured by the s -th image stamped as τ_s .

B. Global Factor Graph Optimization

Finally, a global factor graph would be constructed for continuous-time-based batch optimization, where all initialized states would be refined to global optimal ones. Together five kinds of residuals are involved in the optimization, namely gyroscope residuals and accelerometer residuals for IMUs, Doppler velocity residuals for radars, point-to-surfel residuals for LiDARs, and visual reprojection residuals for cameras.

1) *Gyroscope and Accelerometer Residuals*: The gyroscope and accelerometer residuals have been defined in (26) and (42) as $r_\omega(\tilde{\omega}_n^i)$ and $r_a(\tilde{\mathbf{a}}_n^i)$ respectively, which introduce the optimization of IMU-related spatiotemporal parameters, gravity vector, and B-splines using raw inertial measurements.

2) *Radar Doppler Velocity Residual*: The radar Doppler velocity residual has been defined in (45) as $r_r(\tilde{\mathbf{p}}_n^{r^j}, \tilde{v}_n^{r^j})$, which introduce the optimization of radar-related spatiotemporal parameters and B-splines using raw target measurements.

3) *LiDAR Point-to-Surfel Residual*: When a LiDAR point-to-surfel correspondence is introduced in optimization, a corresponding point-to-surfel residual can be constructed, which could be described as:

$$r_l(\tilde{\mathbf{p}}_n^{l^k}, \mathbf{e}_s^w) \triangleq (\mathbf{n}_s^w)^\top \cdot (\mathbf{R}_{l^k}^w(t_n) \cdot \tilde{\mathbf{p}}_n^{l^k} + \mathbf{p}_{l^k}^w(t_n)) + d_s^w \quad (51)$$

with

$$\begin{aligned} \mathbf{R}_{l^k}^w(\tau) &= \mathbf{R}_{b^r}^w(\tau) \cdot \mathbf{R}_{l^k}^{b^r}, \quad t_n \triangleq \tau_n + \hat{\tau}_{l^k}^{b^r} \\ \mathbf{p}_{l^k}^w(\tau) &= \mathbf{R}_{b^r}^w(\tau) \cdot \mathbf{p}_{l^k}^{b^r} + \mathbf{p}_{b^r}^w(\tau) \end{aligned} \quad (52)$$

where $\mathbf{R}_{b^r}^w(\tau)$ and $\mathbf{p}_{b^r}^w(\tau)$ are quantities obtained from the B-splines. Note that this residual introduces the optimization of LiDAR-related spatiotemporal parameters and B-splines.

4) *Visual Reprojection Residual*: When a visual reprojection correspondence is introduced in optimization, corresponding visual reprojection residuals could be constructed. Given the reprojection correspondence between landmark observation $\tilde{\mathbf{f}}_l^{c^m}$ and $\tilde{\mathbf{f}}_l^{c^m}$, the visual reprojection residual could be described as:

$$r_c(\tilde{\mathbf{f}}_l^{c^m}, \tilde{\mathbf{f}}_l^{c^m}) \triangleq \pi(\mathbf{R}_{c_n}^{c^m} \cdot \mathbf{p}_l^{c^m} + \mathbf{p}_{c_n}^{c^m}, \mathbf{x}_{in}^{c^m}) - \tilde{\mathbf{f}}_l^{c^m} \quad (53)$$

with

$$\begin{aligned} \mathbf{p}_l^{c^m} &= \hat{\beta}^m \cdot \pi^{-1}(\tilde{\mathbf{f}}_l^{c^m}, \hat{\lambda}_l^{c^m}, \mathbf{x}_{in}^{c^m}) \\ \mathbf{T}_{c_n}^{c^m} &\triangleq (\mathbf{T}_{b^r}^w(t_s) \cdot \mathbf{T}_{c_n}^{b^r})^\top \cdot \mathbf{T}_{b^r}^w(t_n) \cdot \mathbf{T}_{c_n}^{b^r} \\ t_{(\cdot)} &\triangleq \tau_{(\cdot)} + \hat{\tau}_{c_n}^{b^r} + \left(\frac{v_l^{c^m}}{h_c} - \frac{1}{2}\right) \times \hat{\tau}_{red}^{c^m}, \quad (\cdot) \simeq n/s \end{aligned} \quad (54)$$

where β^m denotes the global scale of the m -th camera; $\pi^{-1}(\cdot)$ is the pinhole inverse projection function (the inverse operation of $\pi(\cdot)$, see (9)), which projects the 2D image observation to camera frame as a 3D landmark using the camera intrinsics $\mathbf{x}_{in}^{c^m}$ and inverse depth $\lambda_l^{c^m}$. Note that this residual introduces the optimization of camera-related spatiotemporal parameters, visual scale factors, and B-splines.

5) *Continuous-Time Batch Optimization*: Using the residuals from multiple heterogeneous sensors, the final continuous-time batch optimization could be expressed as the following least-squares problem:

$$\begin{aligned} \hat{\mathcal{X}} &= \arg \min \sum_i^{n_b} \sum_n^{\mathcal{D}_\omega^i} \rho_\omega \left(\left\| r_\omega(\tilde{\omega}_n^i) \right\|_{\mathbf{Q}_{\omega,n}^i}^2 \right) \leftarrow \text{Gyro. Mes.} \\ \text{Acce. Mes.} &\rightarrow + \sum_i^{n_b} \sum_n^{\mathcal{D}_a^i} \rho_a \left(\left\| r_a(\tilde{\mathbf{a}}_n^i) \right\|_{\mathbf{Q}_{a,n}^i}^2 \right) \\ \text{Rad. Mes.} &\rightarrow + \sum_j^{n_r} \sum_n^{\mathcal{D}_r^j} \rho_r \left(\left\| r_r(\tilde{\mathbf{p}}_n^{r^j}, \tilde{v}_n^{r^j}) \right\|_{\mathbf{Q}_{r,n}^j}^2 \right) \\ \text{Lidar. Mes.} &\rightarrow + \sum_k^{n_l} \sum_{n,s}^{\mathcal{D}_l^k} \rho_l \left(\left\| r_l(\tilde{\mathbf{p}}_n^{l^k}, \mathbf{e}_s^w) \right\|_{\mathbf{Q}_{l,n,s}^k}^2 \right) \\ \text{Cam. Mes.} &\rightarrow + \sum_m^{n_c} \sum_{l,n,s}^{\mathcal{D}_c^m} \rho_c \left(\left\| r_c(\tilde{\mathbf{f}}_l^{c^m}, \tilde{\mathbf{f}}_l^{c^m}) \right\|_{\mathbf{Q}_{c,l,n,s}^m}^2 \right) \end{aligned} \quad (55)$$

where $\mathbf{Q}_{(\cdot)}$ denotes the information matrix of a residual; $\rho(\cdot)$ are the Cauchy loss functions to reduce outlier influence, especially for dynamic radar targets and inaccurate data association of LiDARs and cameras. The *Ceres solver* [61] is used for solving this nonlinear problem.

C. Multi-Batch Refinement

Considering the high nonlinearity of the continuous-time-based batch optimization problem described in (55), we progressively select parameters to optimize in multiple batches, rather than optimize all parameters together in a batch, to ensure better convergence performance and global optimal.

Specifically, we fix IMU-related spatiotemporal parameters and optimize other ones in the state vector in the first batch, since IMU-related spatiotemporal parameters recovered in the initialization procedure are accurate enough compared with other ones, due to the adequacy of inertial measurements and the rigorousness of initialization. Considering the potential inaccuracy of visual scales recovered in initialization, we also optimize the inverse depth of visual features in the first batch. In the second batch, IMU-related spatiotemporal parameters would be incrementally introduced in the factor graph, and optimized together with other parameters in the state vector. If inertial intrinsics, especially the bias factors, have strong observability, they would also be estimated in this batch. Otherwise, they are required to be pre-calibrated undergoing stationary in a separate process (generally required in the multi-IMU calibration), see Appendix A.

Note that when LiDARs are involved in calibration, the global LiDAR map and the point-to-surfel data association would be reconstructed before each batch optimization based on the estimates from the last optimization, i.e., the LiDAR-related spatiotemporal parameters and B-splines. Considering the accuracy of the global LiDAR map plays an important role in LiDAR-related spatiotemporal determination, another batch optimization (the third one) would be performed when LiDARs are involved, where parameters to be optimized keep the same as the second batch optimization, but are associated with more accurate global LiDAR map and point-to-surfel correspondences in the factor graph.

VII. REAL-WORLD EXPERIMENTS

To verify the feasibility and performance of the proposed calibration method, sufficient real-world experiments are carried out, where both self-collected and public datasets are considered. To ensure the evaluation adequacy, we performed calibration experiments on four kinds of minimum primitives of multi-sensor integration, namely (i) **M-I**: IMU-only multi-IMU, (ii) **M-RI**: multi-radar multi-IMU, (iii) **M-LI**: multi-LiDAR multi-IMU, (iv) **M-CI**: multi-camera multi-IMU, and the maximum multi-sensor integration, namely (v) **M-CLRI**: multi-camera multi-LiDAR multi-radar multi-IMU. Note that the proposed resilient calibration method not only supports such five kinds of sensor suites, but also other ones, see Fig. 1. We only consider such five kinds of sensor suites in the following experiments, as they are the most descriptive suites on resilient calibration performance in *iKalibr*.

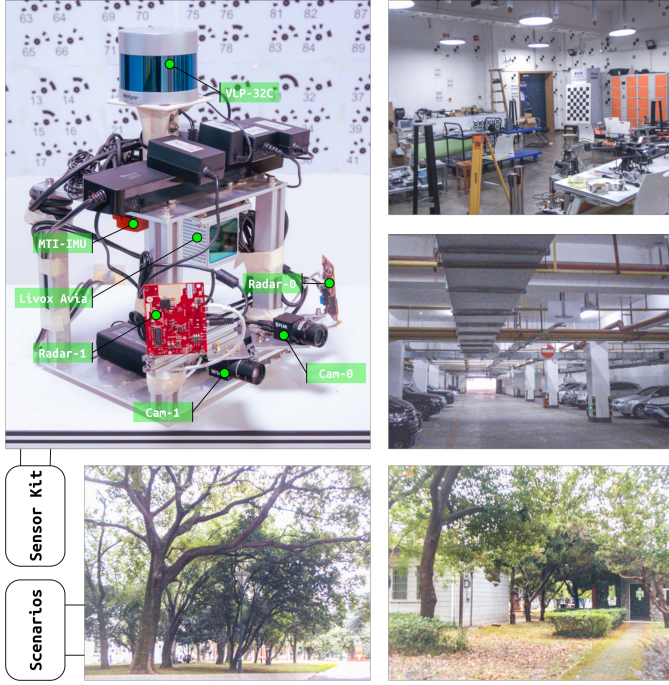


Fig. 9. The self-assembled sensor suite and typical scenarios in real-world experiments. Scenario images are picked from those that cameras captured.

A. Dataset

1) *Our Dataset*: Although a wealth of multi-sensor datasets orienting to localization and mapping evaluation are public, and available for motion-based targetless spatiotemporal calibration, in most of which the platform undergoes insufficiently excited stable motion, and could not support high-accuracy observability-unconstrained calibration. Considering this, we assembled a hardware platform shown in Fig. 9, for a reliable spatiotemporal evaluation on the proposed *iKalibr*. The platform integrates two FLIR cameras (denoted as *Cam-0* and *Cam-1*), a Velodyne VLP-32C LiDAR (denoted as *LiDAR-0*), a Livox Avia LiDAR (denoted as *LiDAR-1*), two TI AWR1843 3D Radars (denoted as *Rad-0* and *Rad-1*), a MTI-G-710 MEMS IMU (denoted as *IMU-0*), and a Livox Avia built-in MEMS IMU (denoted as *IMU-1*). The acquisition rate for cameras, LiDARs, and radars is set to 10 Hz, as for *IMU-0* and *IMU-1*, rates are set to 400 Hz and 200 Hz, respectively. All sensors are only software-synchronized, thus unknown constant time offsets exist, whose determination would be considered in calibration.

To ensure the completeness of the evaluation, several scenarios are encompassed in experiments, covering indoor and outdoor, large and small scales, and structured and structured-less cases, see Fig. 9. Data sequences lasting 30 to 60 seconds were collected in each scenario for experiment evaluation.

2) *Public Dataset*: While our datasets are open-sourced, to strengthen the evaluation reliability further, we also involved three public datasets that meet the demand for motion-based targetless calibration in experiments:

- 1) *LI-Calib* dataset [30]: contains ten data sequences collected handheld in both indoor (garage) and outdoor (court) scenarios. The self-assembled sensor rig inte-

TABLE II
SPATIOTEMPORAL CALIBRATION RESULTS IN M-I EXPERIMENTS

Method		Ours	Mix-Cal [50]	Pseudo GT	
Our Dataset	IMU-0 (Livox)	\hat{p}_x	2.901± 0.061	2.913±0.097	X
		\hat{p}_y	-12.280± 0.044	-12.251±0.080	X
		\hat{p}_z	-3.199± 0.039	-3.148±0.055	X
	IMU-1	$\hat{\theta}_r$	-179.795± 0.013	-179.787±0.047	X
		$\hat{\theta}_p$	-0.462± 0.036	-0.474±0.079	X
		$\hat{\theta}_y$	-87.599±0.149	-87.615± 0.118	X
		$\hat{\tau}$	1.007±0.196	X	X
LI-Calib Dataset [30]	IMU-1	\hat{p}_x	-9.063± 0.054	-9.088±0.085	-9.350
		\hat{p}_y	10.104± 0.055	10.215±0.066	10.100
		\hat{p}_z	0.049±0.048	0.080± 0.047	0.000
	IMU-2	$\hat{\theta}_r$	-0.114± 0.021	-0.095±0.055	0.000
		$\hat{\theta}_p$	0.207± 0.034	0.194±0.091	0.000
		$\hat{\theta}_y$	-0.658± 0.023	-0.663±0.037	0.000
	IMU-0	\hat{p}_x	-17.576± 0.050	-17.458±0.081	X
		\hat{p}_y	-7.633±0.052	-7.557± 0.029	X
		\hat{p}_z	-0.040±0.050	0.019± 0.037	0.000
	IMU-1	$\hat{\theta}_r$	-0.128± 0.024	-0.174±0.146	X
		$\hat{\theta}_p$	0.636± 0.057	0.688±0.080	X
		$\hat{\theta}_y$	-135.941± 0.020	-135.965±0.085	-135.000

* Extrinsic translations in (cm), extrinsic Euler angles in (deg), and time offsets in (ms). All parameters are with respect to IMU-0. Pseudo GTs are rough references from CAD provided by [30].

grates three XSens-100 IMUs (denoted as *IMU-0*, *IMU-1*, and *IMU-2*) sampled at 400 Hz and a Velodyne VLP-16 LiDAR sampled at 10 Hz. This dataset would be utilized in the **M-I** and **M-LI** experiments. Sensors except the LiDAR are hardware-synchronized.

- 2) *TUM GS-RS* dataset [62]: contains ten data sequences collected handheld in the indoor scenarios. The self-assembled sensor rig integrates two uEye UI-3241LE-M-GL cameras (denoted as *Cam-0* and *Cam-1*) sampled at 20 Hz and a Bosch BMI160 IMU sampled at 200 Hz. The *Cam-0* runs in GS mode and the *Cam-1* in RS mode. This dataset would be utilized in the **M-CI** experiment. Sensors are hardware-synchronized.
- 3) *River* dataset [63]: contains three data sequences collected handheld in indoor scenario. The self-assembled sensor rig integrates two AWR1843BOOST 3D radars (denoted as *Rad-0* and *Rad-1*) sampled at 10 Hz and an XSens MTI-G-710 MESE IMU sampled at 400 Hz. This dataset would be utilized in the **M-RI** experiment. Sensors are only software-synchronized.

B. IMU-Only Multi-IMU (M-I) Calibration

1) *Quantitative Evaluation and Comparison*: In this experiment, two datasets, namely *LI-Calib* dataset [30] and ours, are utilized. Three IMUs in *LI-Calib* dataset are hardware-synchronized, thus temporal parameters were fixed as zeros in calibration. As for our dataset, IMUs are only software-synchronized, and temporal estimation was involved. Due to the weak observability of inertial intrinsics in IMU-only multi-IMU calibration, intrinsics were pre-calibrated, see Appendix A. Considering the lack of intrinsic calibration data in *LI-Calib* dataset, inertial intrinsics in *LI-Calib* dataset are obtained from multi-LiDAR multi-IMU calibration, see Section VII-D.

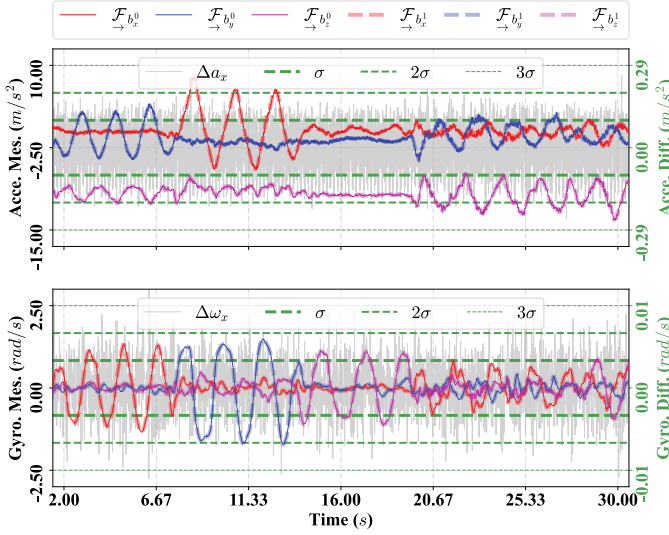


Fig. 10. Inertial measurements (colored) of two IMUs aligned to the coordinate frame of the reference IMU, i.e., the *IMU-0* here, and their difference (gray, only x-axis is plotted). As multiple IMUs are rigidly connected, their inertial measurements aligned to a unique frame are expected to be the same.

The proposed *iKalibr* is compared with *Mix-Cal* [50], a state-of-the-art IMU-only dual-IMU extrinsic calibration method. As inertial time offsets exist in our dataset, to make a fair comparison, inertial measurements given to spatial-only *Mix-Cal* are pre-synchronized based on the time offsets calibrated by *iKalibr*. Meanwhile, frequencies of two IMUs in our dataset are pre-processed to 200 Hz, to meet the requirement of *Mix-Cal*. Table II provides the final calibration results, summarizing spatiotemporal estimates and corresponding standard deviations (STDs). As can be seen, the difference of estimates from *Mix-Cal* and ours is less than 0.1 cm for translation and 0.1 deg for rotation. Regarding repeatability, *iKalibr* achieves average STDs of 0.05 cm for translation, 0.05 deg for rotation, and 0.2 ms for time offset, outperforming *Mix-Cal* in general.

2) *Kinematic Consistency Evaluation*: To make a better presentation of calibration results, using the estimated spatiotemporal parameters and B-splines, we transformed raw inertial measurements of multiple IMUs to a unique coordinate frame, see Fig. 10. As can be seen, inertial measurements of two IMUs transformed to the same frame match each other well. The STDs of inertial difference are about 0.1 m/s² for specific force and 0.03 rad/s for angular velocity. These results demonstrate the superior calibration accuracy and consistency of *iKalibr*.

C. Multi-Radar Multi-IMU (M-RI) Calibration

1) *Quantitative Evaluation and Comparison*: In this experiment, *River* dataset [63] and ours are utilized for calibration evaluation. The state-of-the-art radar-inertial odometer with online extrinsic calibration, namely *X-RIO* [14], is considered in comparison. *X-RIO* supports multi-radar single-IMU sensor configuration, which is employed in this evaluation. Specifically, multiple radars are grouped with each IMU as a kit to perform solving in *X-RIO*. Same as *Mix-Cal*, measurements given to *X-RIO* are temporally pre-synchronized. Meanwhile,

TABLE III
SPATIOTEMPORAL CALIBRATION RESULTS IN M-RI EXPERIMENTS

Method		Ours	X-RIO [14]	Pseudo GT	
Our Dataset	IMU-1 (Livox)	\hat{p}_x	3.193±0.067	5.301±2.377	✗
		\hat{p}_y	-12.132±0.095	-13.525±1.728	✗
		\hat{p}_z	-3.166±0.106	-3.802±1.611	✗
		$\hat{\theta}_r$	-179.764±0.019	-178.851±0.900	✗
		$\hat{\theta}_p$	-0.453±0.026	-2.047±0.815	✗
		$\hat{\theta}_y$	-87.535±0.143	-88.673±1.018	✗
		$\hat{\tau}$	0.967±0.184	✗	✗
	Rad-0	\hat{p}_x	-15.236±0.785	-15.710±1.253	✗
		\hat{p}_y	-22.647±0.710	-22.091±1.559	✗
		\hat{p}_z	6.536±0.702	6.866±0.982	✗
		$\hat{\theta}_r$	174.599±1.054	174.597±0.754	✗
		$\hat{\theta}_p$	8.563±0.641	8.701±0.622	✗
		$\hat{\theta}_y$	-133.296±0.315	-133.365±0.698	✗
		$\hat{\tau}$	-118.777±1.139	✗	✗
	Rad-1	\hat{p}_x	15.551±1.380	15.477±1.821	✗
		\hat{p}_y	-20.631±0.882	-20.194±0.910	✗
		\hat{p}_z	-0.056±0.492	-0.165±1.315	✗
	$\hat{\theta}_r$	-176.790±0.964	-176.242±0.872	✗	
	$\hat{\theta}_p$	4.533±0.792	4.702±0.833	✗	
	$\hat{\theta}_y$	-42.018±0.373	-41.829±0.774	✗	
	$\hat{\tau}$	-119.172±2.123	✗	✗	
River Dataset [63]	Rad-0	\hat{p}_x	12.912±0.565	13.022±1.365	12.495
		\hat{p}_y	-26.172±0.290	-26.021±2.190	-25.812
		\hat{p}_z	17.507±0.363	17.011±1.820	18.146
		$\hat{\theta}_r$	1.551±1.264	2.191±0.810	3.545
		$\hat{\theta}_p$	-7.113±0.661	-7.018±0.721	-7.909
		$\hat{\theta}_y$	-41.955±0.670	-41.720±0.919	-42.184
		$\hat{\tau}$	-115.837±3.748	✗	-115.909
	Rad-1	\hat{p}_x	12.649±0.865	13.208±1.960	12.890
		\hat{p}_y	6.455±0.407	7.051±2.111	6.533
		\hat{p}_z	16.373±1.010	15.801±2.016	16.622
		$\hat{\theta}_r$	-0.398±0.779	-0.299±0.810	-0.818
		$\hat{\theta}_p$	-1.279±1.625	-1.023±1.117	-2.236
		$\hat{\theta}_y$	49.051±0.293	49.602±0.612	48.511
		$\hat{\tau}$	-113.701±0.935	✗	-117.536

* Extrinsic translations in (cm), extrinsic Euler angles in (deg), and time offsets in (ms). All parameters are with respect to IMU-0. Pseudo GTs are rough references provided by [63].

the initial spatial guesses given to *X-RIO* are initialization results of *iKalibr*. Table III provides the final calibration results, summarizing spatiotemporal estimates and corresponding STDs. As can be seen, estimates of two methods are close, while *iKalibr* achieves better repeatability than *X-RIO*. The average STDs of estimates of *iKalibr* are about 0.8 cm for radar translation, 0.8 deg for radar rotation, and 1.8 ms for time offsets. Additionally, compared with spatiotemporal parameters of IMUs, those of radars are poorer, as the noise level of radar target measurements is generally much larger than that of inertial measurements.

2) *Qualitative Evaluation via Doppler Error*: Based on the estimated B-splines and raw radar target measurements, we computed the B-spline-derived Doppler velocities for targets and compared them with the radar-measured ones. Fig. 11 shows the distribution of Doppler errors in one multi-radar multi-IMU calibration in *iKalibr*. Overall, the Doppler errors obey normal distribution, and the average STD is about 0.25 m/s. In particular, the Doppler error distribution of *Rad-*

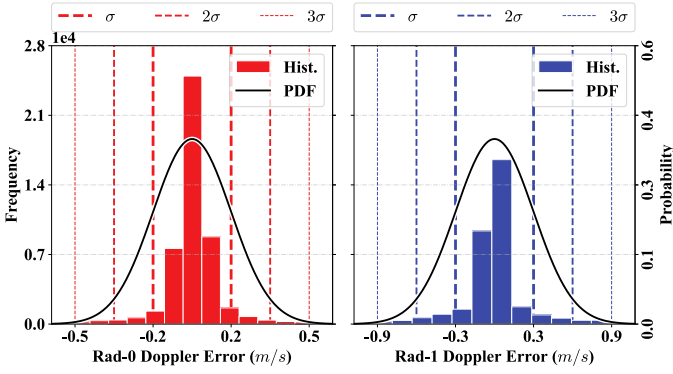


Fig. 11. The Histograms and probability density functions (PDFs) of Doppler errors for multiple radars.

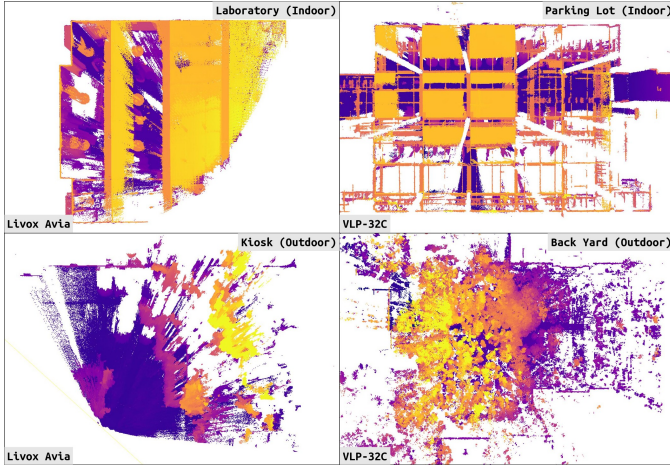


Fig. 12. The final LiDAR maps (bird eye view, parallel projection) from multi-LiDAR multi-IMU calibration in *iKalibr*. Maps are colorized along the direction of the estimated gravity vector.

I is poorer than that of *Rad-0*, which matches the calibration results in Table III. This is mainly related to (i) different radar-detectable object distribution in space when acquiring data, and (ii) different orientations of two radars, see Fig. 9.

D. Multi-LiDAR Multi-IMU (M-LI) Calibration

1) *Quantitative Evaluation and Comparison*: In this experiment, the open-sourced *LI-Calib* dataset [30] is involved in calibration evaluation, which had been utilized in IMU-only multi-IMU evaluation (see Section VII-B). The state-of-the-art single-LiDAR single-IMU spatiotemporal calibration method, namely *OA-Calib* [21], a follow-up work of *LI-Calib* [30] with additional observability-aware module, is considered in comparison. Table IV provides the calibration results, summarizing spatiotemporal estimates and corresponding STDs. It can be seen that for inertial spatiotemporal calibration, *iKalibr* generally outperforms *OA-Calib* in terms of repeatability (see STDs). Such superiority comes from the one-shot calibration of *iKalibr*, which avoids multiple separate single-LiDAR single-IMU calibration procedures, thus capable of better consistency. Note that the small FoV solid-state Livox LiDARs are not yet supported in *OA-Calib*, thus calibration results of Livox Avia are compared with manufacturer-

TABLE IV
SPATIOTEMPORAL CALIBRATION RESULTS IN M-LI EXPERIMENTS

Method		Ours	OA-Calib [30]	Pseudo GT		
Our Dataset	LiDAR-0 (Livox)	\hat{p}_x	2.901±0.060	2.725±0.329	✗	
		\hat{p}_y	-12.292±0.048	-12.428±0.433	✗	
		\hat{p}_z	-3.195±0.037	-3.320±0.206	✗	
	IMU-1	$\hat{\theta}_r$	-179.800±0.019	-179.924±0.175	✗	
		$\hat{\theta}_p$	-0.453±0.029	-0.406±0.143	✗	
		$\hat{\theta}_y$	-87.601±0.150	-87.624±0.145	✗	
		$\hat{\tau}$	1.056±0.235	1.574±0.891	✗	
	LiDAR-0 (VLP)	\hat{p}_x	-0.479±0.274	-0.501±0.529	✗	
		\hat{p}_y	-4.960±0.115	-5.352±0.478	✗	
		\hat{p}_z	-21.839±0.581	-21.839±0.923	✗	
		$\hat{\theta}_r$	-179.785±0.041	-179.792±0.034	✗	
		$\hat{\theta}_p$	0.103±0.025	0.149±0.042	✗	
		$\hat{\theta}_y$	2.098±0.138	2.115±0.153	✗	
		$\hat{\tau}$	7.190±0.039	7.927±0.892	✗	
	LI-Calib Dataset [30]	LiDAR-1 (Livox)	\hat{p}_x	1.188±1.033	✗	4.165
			\hat{p}_y	2.592±0.310	✗	2.326
\hat{p}_z			-2.260±0.237	✗	-2.840	
IMU-1		$\hat{\theta}_r$	-1.203±0.025	✗	0.000	
		$\hat{\theta}_p$	-0.582±0.039	✗	0.000	
		$\hat{\theta}_y$	-0.324±0.023	✗	0.000	
		$\hat{\tau}$	6.792±0.235	✗	✗	
IMU-2		\hat{p}_x	-9.173±0.056	-9.082±0.360	-9.350	
		\hat{p}_y	10.109±0.042	10.237±0.310	10.100	
		\hat{p}_z	0.059±0.052	0.652±0.542	0.000	
IMU-1		$\hat{\theta}_r$	-0.115±0.022	-0.248±0.074	0.000	
		$\hat{\theta}_p$	0.210±0.040	-0.076±0.171	0.000	
		$\hat{\theta}_y$	-0.659±0.017	-0.640±0.052	0.000	
IMU-2		\hat{p}_x	-17.673±0.059	-17.271±0.531	✗	
		\hat{p}_y	-7.619±0.044	-7.241±0.340	✗	
		\hat{p}_z	-0.028±0.052	0.494±0.613	00.000	
IMU-1	$\hat{\theta}_r$	-0.131±0.031	0.794±0.042	✗		
	$\hat{\theta}_p$	0.633±0.059	0.160±0.055	✗		
	$\hat{\theta}_y$	-135.947±0.017	-135.97±0.098	-135.000		
LiDAR	\hat{p}_x	-10.739±0.153	-9.975±0.501	✗		
	\hat{p}_y	0.078±0.099	0.015±0.311	✗		
	\hat{p}_z	14.775±0.551	13.440±0.442	✗		
LiDAR	$\hat{\theta}_r$	-0.176±0.045	-0.232±0.041	✗		
	$\hat{\theta}_p$	0.291±0.031	0.213±0.062	✗		
	$\hat{\theta}_y$	90.839±0.030	90.896±0.073	✗		
	$\hat{\tau}$	8.926±0.759	8.874±0.753	✗		

* Extrinsic translations in (cm), extrinsic Euler angles in (deg), and time offsets in (ms). All parameters, except those of Livox LiDAR, are with respect to IMU-0. GTs of Livox LiDAR (with respect to its built-in IMU) are from the sensor manufacturer, and GTs of LI-Calib dataset are rough references from CAD provided by [30].

provided reference. Interestingly, it can be found that the y-axis and z-axis translation results of Livox Avia LiDAR are well calibrated, matching well with the reference and having small STDs, the x-axis translation is poorly calibrated with a large STD. This is mainly related to (i) insufficient forward motion excitation (see Fig. 10) and (ii) the lack of rear point-to-surfel constraints (see Fig. 12). As for Velodyne LiDARs, namely the VLP-16 in *LI-Calib* dataset and the VLP-32C in our dataset, *iKalibr* achieves comparable calibration results with *OA-Calib*, and has a slight advantage in repeatability.

2) *Qualitative Evaluation via By-Products*: Based on estimated B-splines and gravity vector, calibrated spatiotemporal parameters, and raw LiDAR measurements, gravity-aligned LiDAR maps can be constructed, see Fig. 12. It can be found

TABLE V
SPATIOTEMPORAL CALIBRATION RESULTS IN M-CI EXPERIMENTS

Method			Ours	Kalibr [29]	Mean Diff.	
Our Dataset	IMU-1	\hat{p}_x	2.898±0.054	2.920± 0.003	0.022	
		\hat{p}_y	-12.286± 0.050	-12.166±0.094	0.120	
		\hat{p}_z	-3.195± 0.042	-3.146±0.089	0.049	
		$\hat{\theta}_r$	-179.797±0.021	-179.820± 0.004	0.023	
		$\hat{\theta}_p$	-0.451±0.035	-0.379± 0.008	0.072	
		$\hat{\theta}_y$	-87.601±0.148	-87.515± 0.032	0.086	
	Cam-0	$\hat{\tau}$	1.032±0.351	0.750± 0.062	0.282	
		\hat{p}_x	7.495±0.207	7.941± 0.128	0.446	
		\hat{p}_y	-24.997±0.205	-25.630± 0.016	0.633	
		\hat{p}_z	11.956±0.165	12.219± 0.003	0.263	
		$\hat{\theta}_r$	-93.227±0.043	-93.245± 0.016	0.018	
		$\hat{\theta}_p$	-0.225± 0.007	-0.212±0.012	0.043	
	Cam-1	$\hat{\theta}_y$	-177.706±0.124	-177.621± 0.065	0.085	
		$\hat{\tau}$	-22.816±0.347	-23.300± 0.141	0.484	
Cam-1		\hat{p}_x	-6.618±0.239	-6.903± 0.051	0.285	
		\hat{p}_y	-25.501±0.176	-26.467± 0.005	0.966	
		\hat{p}_z	11.800±0.344	11.765± 0.075	0.035	
		$\hat{\theta}_r$	94.227±0.052	94.109± 0.001	0.118	
	$\hat{\theta}_p$	-0.490±0.012	-0.519± 0.004	0.029		
	$\hat{\theta}_y$	4.549±0.129	4.619± 0.045	0.070		
TUM GS-RS Dataset [62]	Cam-0 (GS)	$\hat{\tau}$	-8.810±0.890	-9.461± 0.134	0.651	
		\hat{p}_x	0.324±0.300	0.780 [62]	0.456	
		\hat{p}_y	5.338±0.246	5.214 [62]	0.123	
	Cam-0 (GS)	\hat{p}_z	-4.394±0.611	-4.284 [62]	0.109	
		Cam-1 (RS)	$\hat{\theta}_r$	179.630±0.088	179.645 [62]	0.015
			$\hat{\theta}_p$	-0.339±0.040	-0.424 [62]	0.085
	$\hat{\theta}_y$		-90.334±0.012	-90.341 [62]	0.007	
	Cam-1 (RS)	\hat{p}_x	0.464±0.254	0.699 [62]	0.235	
		\hat{p}_y	-5.753±0.157	-5.708 [62]	0.044	
		\hat{p}_z	-4.228±0.533	-4.227 [62]	0.001	
	Cam-1 (RS)	$\hat{\theta}_r$	179.430±0.077	179.370 [62]	0.059	
		$\hat{\theta}_p$	-0.272±0.030	-0.241 [62]	0.030	
		$\hat{\theta}_y$	-90.162±0.011	-90.158 [62]	0.003	
			$\hat{\tau}_{red}$	30.554±0.116	30.177 [62]	0.376

* Extrinsic translations in (cm), extrinsic Euler angles in (deg), and time offsets in (ms). All parameters are with respect to IMU-0. Calibration results of Kalibr in TUM dataset are from [62].

that structural details of surroundings could be visible, and the color of objects coincides with corresponding elevations. These results demonstrate the superior consistency of *iKalibr*.

E. Multi-Camera Multi-IMU (M-CI) Calibration

1) *Quantitative Evaluation and Comparison*: In this experiment, the TUM GS-RS dataset [62] is involved in the evaluation, together with our dataset, mainly as a supplement to RS camera (the readout time) calibration evaluation. To make a reliable comparison, the well-known chessboard-based visual-inertial spatiotemporal calibration toolkit, namely *Kalibr* [29], is considered in the experiment. Table V provides the calibration results, summarizing spatiotemporal estimates and corresponding STDs. It can be found that the proposed *iKalibr* can generate comparable calibration results with *Kalibr*. The estimate differences between *Kalibr* and ours are about 1 cm for translation, 0.1 deg for rotation, and 0.8 ms for time offset. More specifically, *Kalibr* is superior to *iKalibr* in translation calibration (see STDs). This is reasonable as the target-based *Kalibr* could explicitly obtain accurate scale priori

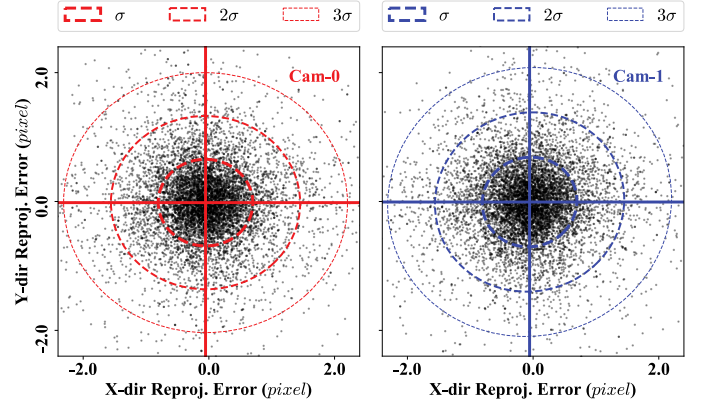


Fig. 13. The distribution of visual reprojection errors for multiple cameras. Solid lines represent means of reprojection errors.

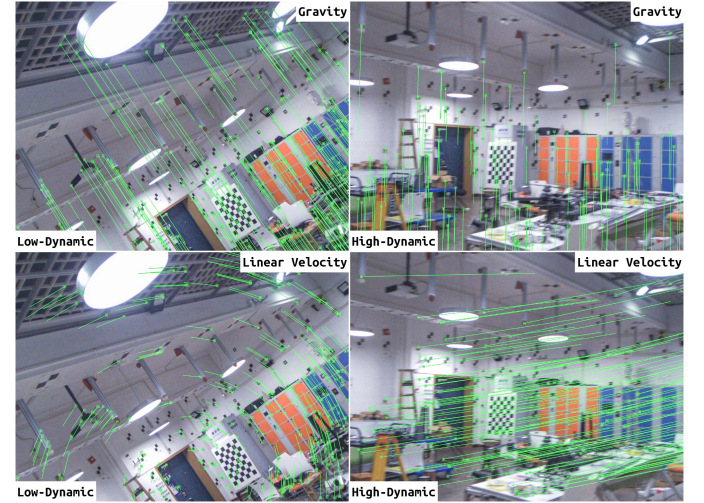


Fig. 14. The visual kinematics of high and low dynamic moments in our Laboratory dataset. Kinematics coincides with the structural details and motion blur (see chessboard). Tails of features in images represent gravity vectors or linear velocities.

from the chessboard, while the target-free *iKalibr* estimates visual scale using linear acceleration information from IMU. In terms of readout time determination of RS camera (TUM GS-RS dataset), the difference between the reference and our estimated one is less than 0.5 ms, with a STD of 0.15 ms.

2) *Qualitative Evaluation via By-Products*: Based on the estimated B-splines, inverse depths of features, and feature matching correspondences, we computed the visual reprojection errors for each camera (TUM GS-RS dataset, sequence 1), see Fig. 13. It can be found that errors obey zero-mean Gaussian distribution, and STDs for both GS and RS cameras are within 1 pixel. We also projected the visual kinematics (gravity vectors and linear velocities of landmarks) to each image to validate estimation consistency, see Fig. 14. As can be seen, the direction of estimated gravity matches well with the structures of the surroundings. The motion blur of images coincides with different dynamic motions (see chessboard).

TABLE VI
SPATIOTEMPORAL CALIBRATION RESULTS IN M-CLRI EXPERIMENTS

Sensor	Extrinsic Translation (<i>cm</i>)			Extrinsic Rotation (<i>deg</i>)			Temporal Param. (<i>ms</i>)
	\hat{p}_x	\hat{p}_y	\hat{p}_z	$\hat{\theta}_r$	$\hat{\theta}_p$	$\hat{\theta}_y$	
IMU-1	2.908±0.061	-12.297±0.049	-3.185±0.038	-179.793±0.014	-0.462±0.039	-87.599±0.151	1.128±0.270
Rad-0	-15.016±1.587	-22.891±0.810	6.524±0.709	174.333±1.120	8.643±1.134	-133.398±0.280	-118.798±1.176
Rad-1	15.376±1.643	-20.846±0.866	-0.057±0.429	-176.786±1.499	4.397±0.607	-41.529±0.392	-119.171±1.651
LiDAR-0	-0.571±0.174	-4.925±0.093	-21.693±0.579	-179.787±0.040	0.105±0.027	2.093±0.141	7.193±0.034
LiDAR-1	0.378±0.303	-13.753±1.085	-0.858±0.300	178.994±0.011	0.120±0.026	-87.273±0.141	7.844±0.065
Cam-0	7.386±0.214	-25.287±0.274	11.828±0.285	-93.182±0.046	-0.221±0.008	-177.706±0.138	-22.787±0.327
Cam-1	-6.640±0.182	-25.902±0.284	11.732±0.416	94.188±0.054	-0.497±0.012	4.556±0.139	-8.784±0.850

* Extrinsic translations in (*cm*), extrinsic Euler angles in (*deg*), and time offsets in (*ms*). All parameters are with respect to IMU-0.



Fig. 15. Raw images and their covisible inverse depth images sharing the same camera perspectives. Inverse Depth images are created by projecting LiDAR points to image planes based on camera intrinsics, the estimated spatiotemporal parameters, and global LiDAR map.

F. One-Shot Multi-Sensor (*M-CLRI*) Calibration

1) *Quantitative Evaluation and Convergence Performance*: While the previous experiments evaluated *iKalibr* on four kinds of minimum primitives of multi-sensor inertial integration, the most notable feature of *iKalibr* is supporting one-shot multi-sensor spatiotemporal determination, as long as the sensor kit satisfies (1). Table VI provides the final results, including the estimates and their STDs. It can be found that among four kinds of sensors, the IMUs achieve the optimal repeatability, followed by cameras and LiDARs, and radars have the worst repeatability. This is largely related to the measuring noise levels of the sensors themselves. The convergence performance of spatiotemporal parameters in one-shot calibration is shown in Fig. 16. Due to the designed initialization procedure and multi-stage refinement, spatiotemporal parameters can steadily converge to final states.

2) *Qualitative Evaluation via By-Products*: When camera and LiDAR are involved in calibration, covisible inverse depth images can be created using the LiDAR map, B-splines, and camera intrinsics, see Fig. 15, for a qualitative calibration consistency evaluation. It's clear that the depth information matches well with the raw images, which indicates the excellent consistency of the proposed *iKalibr*.

VIII. CONCLUSION AND FUTURE WORK

In this work, we propose a unified target-free spatiotemporal calibration framework orienting to resilient integrated inertial

systems, termed as *iKalibr*, which supports both spatial and temporal determination, enables one-shot resilient and compact calibration, and requires no additional artificial target or aiding sensor. Considering the high nonlinearity of continuous-time-based batch spatiotemporal optimization, a rigorous initialization is first conducted to recover accurate initial guesses of all parameters in estimator. Following that, a continuous-time-based graph optimization is organized based on raw measurements, data correspondences, and initials of states. The graph optimization would be performed several times until the final convergence, to steadily refine all states to global optimal ones. Sufficient real-world experiments are performed, and the results show that *iKalibr* is capable of accurate and consistent resilient spatiotemporal calibration. The IMU, radar, LiDAR, and optimal camera are supported currently in *Kalibr*. In future work, we will further the computational efficiency of *Kalibr* and support more types of sensors, such as the event cameras.

APPENDIX A

STATIONARY INERTIAL INTRINSIC CALIBRATION

When performing IMU-only multi-IMU spatiotemporal calibration in *iKalibr*, the intrinsics of the IMU, namely \mathbf{x}_{in}^b , are with weak observability, which could lead to the problem rank deficient and further adversely affects the spatiotemporal determination. Considering this, the intrinsics are expected to be pre-calibrated using a separate process, and would be set

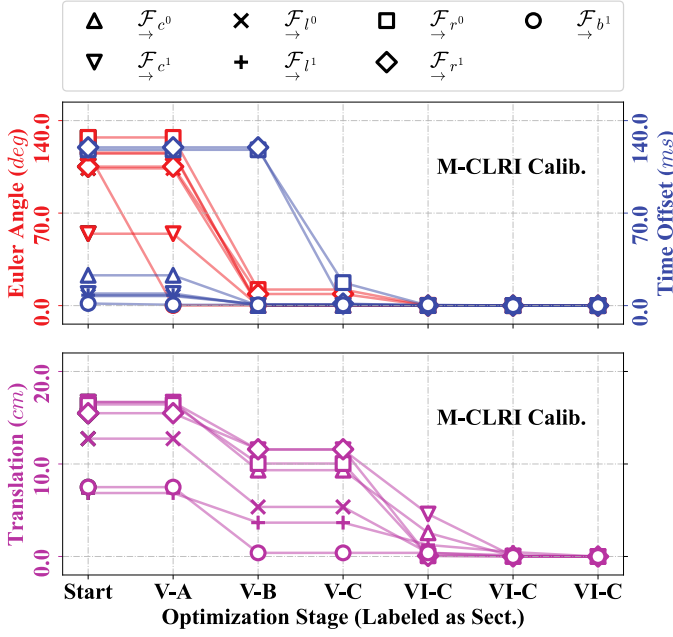


Fig. 16. The convergence performance of spatiotemporal optimization in **M-CLRI** calibration, where all parameters are with respect to *IMU-0*. Quantities are the RMSEs of estimates with respect to the final ones. For better readers' understanding, each stage is labeled by its corresponding section index.

to constants and not optimized in spatiotemporal optimization. Specifically, given the inertial measurement of \vec{F}_b , we can associate them with the world-frame angular velocity and linear acceleration as:

$$\begin{aligned} \mathbf{a}(\tau) &= (\mathbf{R}_b^w(\tau))^T \cdot (\mathbf{a}_b^w(\tau) - \mathbf{g}^w) \\ \boldsymbol{\omega}(\tau) &= (\mathbf{R}_b^w(\tau))^T \cdot \boldsymbol{\omega}_b^w(\tau) \end{aligned} \quad (56)$$

When the body is stationary, we have the following approximation:

$$\mathbf{R}_b^w(\tau) \equiv \mathbf{I}_{3 \times 3}, \mathbf{a}_b^w(\tau) \equiv \mathbf{0}_{3 \times 1}, \boldsymbol{\omega}_b^w(\tau) \equiv \mathbf{0}_{3 \times 1}. \quad (57)$$

Although the body is not strictly stationary with respect to the inertial space and would lead to trace angular velocity and linear acceleration due to the rotation of the earth, (57) still holds for MEMS IMUs this work focuses on, since their high noise level would drown out such perception. Based on the stationary inertial measurements collected under several poses (generally six symmetric poses), the following constraint would be constructed for each stationary data piece for intrinsic determination:

$$\hat{\mathbf{x}}_{\text{in}}^b = \arg \min \sum_i \sum_n \left(\|r_\omega(\tilde{\boldsymbol{\omega}}_{i,n})\|_{\mathbf{Q}_{i,n}}^2 + \|r_a(\tilde{\mathbf{a}}_{i,n})\|_{\mathbf{Q}_{i,n}}^2 \right) \quad (58)$$

with

$$\begin{aligned} r_\omega(\tilde{\boldsymbol{\omega}}_{i,n}) &\triangleq h_\omega(\mathbf{0}_{3 \times 1}, \hat{\mathbf{x}}_{\text{in}}^b) - \tilde{\boldsymbol{\omega}}_{i,n} \\ r_a(\tilde{\mathbf{a}}_{i,n}) &\triangleq h_a(-\hat{\mathbf{g}}^w, \hat{\mathbf{x}}_{\text{in}}^b) - \tilde{\mathbf{a}}_{i,n} \end{aligned} \quad (59)$$

where \mathcal{D}_i denotes the i -th data piece in the stationary data sequence \mathcal{S}_{sta} ; \mathbf{g}^w is the world-frame gravity vector of the i -th data piece, which would also be estimated in this problem. Note that while all intrinsics of accelerometer can be determined by (58), only the bias of intrinsics for gyroscope

can be calibrated in this problem. Other intrinsic parameters of gyroscope, such as scale and non-orthogonal factors, are without observability. In fact, these unobservable factors are generally calibrated by IMU providers and have been compensated in inertial outputs.

APPENDIX B

SENSOR-INERTIAL ALIGNMENT CONSTRAINTS

The inertial measurement of \vec{F}_b , i.e., body-frame angular velocity and specific force, can be associated with the B-spline-derived world-frame angular velocity and linear acceleration, which is described as follows:

$$\begin{aligned} \mathbf{a}(\tau) &= (\mathbf{R}_b^w(\tau))^T \cdot (\mathbf{a}_b^w(\tau) - \mathbf{g}^w) \\ \boldsymbol{\omega}(\tau) &= (\mathbf{R}_b^w(\tau))^T \cdot \boldsymbol{\omega}_b^w(\tau) \end{aligned} \quad (60)$$

where $\mathbf{R}_b^w(\tau)$, $\boldsymbol{\omega}_b^w(\tau)$, and $\mathbf{a}_b^w(\tau)$ are kinematics from the B-splines. By introducing inertial extrinsics, (60) can be extended to multiple IMUs:

$$\begin{aligned} \mathbf{a}^i(\tau) &= (\mathbf{R}_{b^i}^w(\tau))^T \cdot (\mathbf{a}_{b^i}^w(\tau) - \mathbf{g}^w) \\ \boldsymbol{\omega}^i(\tau) &= (\mathbf{R}_{b^i}^w(\tau))^T \cdot \boldsymbol{\omega}_{b^i}^w(\tau) \end{aligned} \quad (61)$$

with

$$\begin{aligned} \mathbf{R}_{b^i}^w(\tau) &= \mathbf{R}_{b^r}^w(\tau) \cdot \mathbf{R}_{b^i}^{b^r}, \quad \boldsymbol{\omega}_{b^i}^w(\tau) = \boldsymbol{\omega}_{b^r}^w(\tau), \\ \mathbf{a}_{b^i}^w(\tau) &= \mathbf{a}_{b^r}^w(\tau) + \left([\boldsymbol{\alpha}_{b^r}^w(\tau)]_\times + [\boldsymbol{\omega}_{b^r}^w(\tau)]_\times^2 \right) \cdot \mathbf{R}_{b^r}^w(\tau) \cdot \mathbf{p}_{b^i}^{b^r} \end{aligned} \quad (62)$$

where $\mathbf{R}_{b^r}^w(\tau)$, $\boldsymbol{\omega}_{b^r}^w(\tau)$, $\boldsymbol{\alpha}_{b^r}^w(\tau)$, and $\mathbf{a}_{b^r}^w(\tau)$ are kinematics from the B-splines of the reference IMU \vec{F}_{b^r} . By performing time integration on (61), the linear velocity variation in timepiece $[\tau_n, \tau_{n+1})$ can be obtained as:

$$\mathbf{v}_{b^r}^w(\tau_{n+1}) - \mathbf{v}_{b^r}^w(\tau_n) = \mathbf{c}_{n,n+1}^i - \mathbf{A}_{n,n+1}^i \cdot \mathbf{p}_{b^i}^{b^r} + \mathbf{g}^w \cdot \Delta\tau_{n,n+1} \quad (63)$$

with

$$\begin{aligned} \mathbf{c}_{n,n+1}^i &\triangleq \int_{\tau_n}^{\tau_{n+1}} \mathbf{R}_{b^r}^w(t) \cdot \mathbf{R}_{b^i}^{b^r} \cdot \mathbf{a}^i(t) \cdot dt \\ \mathbf{A}_{n,n+1}^i &\triangleq \int_{\tau_n}^{\tau_{n+1}} \left([\boldsymbol{\alpha}_{b^r}^w(t)]_\times + [\boldsymbol{\omega}_{b^r}^w(t)]_\times^2 \right) \cdot \mathbf{R}_{b^r}^w(t) \cdot dt \end{aligned} \quad (64)$$

where $\Delta\tau_{n,n+1} = \tau_{n+1} - \tau_n$. Continuing to perform time integration on (63), the position variation in timepiece $[\tau_n, \tau_{n+1})$ can be obtained as:

$$\begin{aligned} \mathbf{p}_{b^r}^w(\tau_{n+1}) - \mathbf{p}_{b^r}^w(\tau_n) &= \mathbf{d}_{n,n+1}^i - \mathbf{B}_{n,n+1}^i \cdot \mathbf{p}_{b^i}^{b^r} \\ &\quad + \mathbf{v}_{b^r}^w(\tau_n) \cdot \Delta\tau_{n,n+1} + \frac{1}{2} \cdot \mathbf{g}^w \cdot \Delta^2\tau_{n,n+1} \end{aligned} \quad (65)$$

with

$$\begin{aligned} \mathbf{d}_{n,n+1}^i &\triangleq \int_{\tau_n}^{\tau_{n+1}} \int_{\tau_n}^{\tau_{n+1}} \mathbf{R}_{b^r}^w(t) \cdot \mathbf{R}_{b^i}^{b^r} \cdot \mathbf{a}^i(t) \cdot dt^2 \\ \mathbf{B}_{n,n+1}^i &\triangleq \int_{\tau_n}^{\tau_{n+1}} \int_{\tau_n}^{\tau_{n+1}} \left([\boldsymbol{\alpha}_{b^r}^w(t)]_\times + [\boldsymbol{\omega}_{b^r}^w(t)]_\times^2 \right) \cdot \mathbf{R}_{b^r}^w(t) \cdot dt^2 \end{aligned} \quad (66)$$

Note that the right parts in both (63) and (65) could be computed independently for each IMU based on the fitted rotation B-spline, inertial extrinsic rotations and time offsets, and raw specific force measurements in timepiece $[\tau_n, \tau_{n+1})$. Integration items, namely $\mathbf{c}_{n,n+1}^i$, $\mathbf{A}_{n,n+1}^i$, $\mathbf{d}_{n,n+1}^i$, and $\mathbf{B}_{n,n+1}^i$, can be obtained by numerical integration methods, such as midpoint rule, trapezoidal rule, or Simpson's rule [64].

By performing an equivalent transformation on the variation items (left parts) in (63) and (65), additional sensors can be involved to construct sensor-inertial alignment constraints. For example, regarding the radar, $\mathbf{v}_{br}^w(\cdot)$ can be organized based on radar-derived radar-frame linear velocities and extrinsics between the radar and the reference IMU. In terms of the LiDAR and camera, $\mathbf{p}_{br}^w(\cdot)$ can be organized based on odometer-derived positions and extrinsics. As for the IMU, $\mathbf{v}_{br}^w(\cdot)$ in (63) would be treated as estimated quantities explicitly. For more details, see Section V-B.

ACKNOWLEDGMENTS

The calibration data acquisition is performed on the GREAT (GNSS+ REsearch, Application and Teaching) software, developed by the GREAT Group, School of Geodesy and Geomatics (SGG), Wuhan University.

CREDIT AUTHORSHIP CONTRIBUTION STATEMENT

Shuolong Chen: Conceptualisation, Methodology, Software, Validation, Original Draft. **Xingxing Li:** Resources, Supervision, Funding Acquisition, Review And Editing. **Shengyu Li** and **Yuxuan Zhou:** Investigation, Review And Editing. **Xiaoteng Yang:** Data Curation.

REFERENCES

- [1] T. Qin, P. Li, and S. Shen, "Vins-mono: A robust and versatile monocular visual-inertial state estimator," *IEEE Trans. Rob.*, vol. 34, no. 4, pp. 1004–1020, 2018.
- [2] P. Geneva, K. Eickenhoff, W. Lee, Y. Yang, and G. Huang, "Openvins: A research platform for visual-inertial estimation," in *2020 Proc. IEEE Int. Conf. Rob. Autom.* IEEE, 2020, pp. 4666–4672.
- [3] C. Campos, R. Elvira, J. J. G. Rodríguez, J. M. Montiel, and J. D. Tardós, "Orb-slam3: An accurate open-source library for visual, visual-inertial, and multimap slam," *IEEE Trans. Rob.*, vol. 37, no. 6, pp. 1874–1890, 2021.
- [4] T. Shan, B. Englot, D. Meyers, W. Wang, C. Ratti, and D. Rus, "Lio-sam: Tightly-coupled lidar inertial odometry via smoothing and mapping," in *2020 IEEE Int. Conf. Intell. Rob. Syst.* IEEE, 2020, pp. 5135–5142.
- [5] W. Xu, Y. Cai, D. He, J. Lin, and F. Zhang, "Fast-lid2: Fast direct lidar-inertial odometry," *IEEE Trans. Rob.*, vol. 38, no. 4, pp. 2053–2073, 2022.
- [6] T.-M. Nguyen, D. Duberg, P. Jensfelt, S. Yuan, and L. Xie, "Slit: Multi-input multi-scale surfel-based lidar-inertial continuous-time odometry and mapping," *IEEE Robot. Autom.*, vol. 8, no. 4, pp. 2102–2109, 2023.
- [7] A. Kramer, C. Stahoviak, A. Santamaria-Navarro, A.-A. Agha-Mohammadi, and C. Heckman, "Radar-inertial ego-velocity estimation for visually degraded environments," in *2020 Proc. IEEE Int. Conf. Rob. Autom.* IEEE, 2020, pp. 5739–5746.
- [8] Y. Z. Ng, B. Choi, R. Tan, and L. Heng, "Continuous-time radar-inertial odometry for automotive radars," in *2021 IEEE Int. Conf. Intell. Rob. Syst.* IEEE, 2021, pp. 323–330.
- [9] J. Michalczyk, R. Jung, and S. Weiss, "Tightly-coupled ekf-based radar-inertial odometry," in *2022 IEEE Int. Conf. Intell. Rob. Syst.* IEEE, 2022, pp. 12336–12343.
- [10] X. Zuo, Y. Yang, P. Geneva, J. Lv, Y. Liu, G. Huang, and M. Pollefeys, "Lic-fusion 2.0: Lidar-inertial-camera odometry with sliding-window plane-feature tracking," in *2020 IEEE Int. Conf. Intell. Rob. Syst.* IEEE, 2020, pp. 5112–5119.
- [11] J. Lin and F. Zhang, "R3 live: A robust, real-time, rgb-colored, lidar-inertial-visual tightly-coupled state estimation and mapping package," in *2022 Proc. IEEE Int. Conf. Rob. Autom.* IEEE, 2022, pp. 10672–10678.
- [12] C. Zheng, Q. Zhu, W. Xu, X. Liu, Q. Guo, and F. Zhang, "Fast-livo: Fast and tightly-coupled sparse-direct lidar-inertial-visual odometry," in *2022 IEEE Int. Conf. Intell. Rob. Syst.* IEEE, 2022, pp. 4003–4009.
- [13] K. Eickenhoff, P. Geneva, and G. Huang, "Mimic-vins: A versatile and resilient multi-imu multi-camera visual-inertial navigation system," *IEEE Trans. Rob.*, vol. 37, no. 5, pp. 1360–1380, 2021.
- [14] C. Doer and G. F. Trommer, "x-rio: Radar inertial odometry with multiple radar sensors and yaw aiding," *Gyroscopy and Navigation*, vol. 12, no. 4, pp. 329–339, 2021.
- [15] T.-M. Nguyen, S. Yuan, M. Cao, L. Yang, T. H. Nguyen, and L. Xie, "Milion: Tightly coupled multi-input lidar-inertia odometry and mapping," *IEEE Robot. Autom.*, vol. 6, no. 3, pp. 5573–5580, 2021.
- [16] Z. Zhang, "A flexible new technique for camera calibration," *IEEE Trans. Pattern Anal. Mach. Intell.*, vol. 22, no. 11, pp. 1330–1334, 2000.
- [17] E. Olson, "Apriltag: A robust and flexible visual fiducial system," in *2011 Proc. IEEE Int. Conf. Rob. Autom.* IEEE, 2011, pp. 3400–3407.
- [18] W. Liu and Y. Li, "Error modeling and extrinsic-intrinsic calibration for lidar-imu system based on cone-cylinder features," *Rob. Autom. Syst.*, vol. 114, pp. 124–133, 2019.
- [19] J. Oh, K.-S. Kim, M. Park, and S. Kim, "A comparative study on camera-radar calibration methods," in *2018 Int. Conf. Control, Autom., Robot. Vis., ICARCV.* IEEE, 2018, pp. 1057–1062.
- [20] Z. Yang and S. Shen, "Monocular visual-inertial state estimation with online initialization and camera-imu extrinsic calibration," *IEEE Trans. Autom. Sci. Eng.*, vol. 14, no. 1, pp. 39–51, 2016.
- [21] J. Lv, X. Zuo, K. Hu, J. Xu, G. Huang, and Y. Liu, "Observability-aware intrinsic and extrinsic calibration of lidar-imu systems," *IEEE Trans. Rob.*, vol. 38, no. 6, pp. 3734–3753, 2022.
- [22] M. Li and A. I. Mourikis, "Online temporal calibration for camera-imu systems: Theory and algorithms," *Int. J. Rob. Res.*, vol. 33, no. 7, pp. 947–964, 2014.
- [23] J. Huai, Y. Lin, Y. Zhuang, C. K. Toth, and D. Chen, "Observability analysis and keyframe-based filtering for visual inertial odometry with full self-calibration," *IEEE Trans. Rob.*, vol. 38, no. 5, pp. 3219–3237, 2022.
- [24] T. Qin and S. Shen, "Online temporal calibration for monocular visual-inertial systems," in *2018 IEEE Int. Conf. Intell. Rob. Syst.* IEEE, 2018, pp. 3662–3669.
- [25] Y. Yang, P. Geneva, K. Eickenhoff, and G. Huang, "Degenerate motion analysis for aided ins with online spatial and temporal sensor calibration," *IEEE Robot. Autom.*, vol. 4, no. 2, pp. 2070–2077, 2019.
- [26] B. Fu, F. Han, Y. Wang, Y. Jiao, X. Ding, Q. Tan, L. Chen, M. Wang, and R. Xiong, "High-precision multicamera-assisted camera-imu calibration: Theory and method," *IEEE Trans. Instrum. Meas.*, vol. 70, pp. 1–17, 2021.
- [27] S. Mishra, G. Pandey, and S. Saripalli, "Target-free extrinsic calibration of a 3d-lidar and an imu," in *2021 IEEE Int. Conf. Multisensor Fusion Integr. Intell. Syst.* IEEE, 2021, pp. 1–7.
- [28] J. Domhof, J. F. Kooij, and D. M. Gavrila, "A joint extrinsic calibration tool for radar, camera and lidar," *IEEE Trans. Intell. Veh.*, vol. 6, no. 3, pp. 571–582, 2021.
- [29] P. Furgale, J. Rehder, and R. Siegwart, "Unified temporal and spatial calibration for multi-sensor systems," in *2013 IEEE Int. Conf. Intell. Rob. Syst.* IEEE, 2013, pp. 1280–1286.
- [30] J. Lv, J. Xu, K. Hu, Y. Liu, and X. Zuo, "Targetless calibration of lidar-imu system based on continuous-time batch estimation," in *2020 IEEE Int. Conf. Intell. Rob. Syst.* IEEE, 2020, pp. 9968–9975.
- [31] J. Huai, Y. Zhuang, Y. Lin, G. Jozkow, Q. Yuan, and D. Chen, "Continuous-time spatiotemporal calibration of a rolling shutter camera-imu system," *IEEE Sensors J.*, vol. 22, no. 8, pp. 7920–7930, 2022.
- [32] C. Sommer, V. Usenko, D. Schubert, N. Demmel, and D. Cremers, "Efficient derivative computation for cumulative b-splines on lie groups," in *Proc. IEEE Comput. Soc. Conf. Comput. Vision Pattern Recognit.*, 2020, pp. 11148–11156.
- [33] J. Johnson, J. Mangelson, T. Barfoot, and R. Beard, "Continuous-time trajectory estimation: A comparative study between gaussian process and spline-based approaches," *arXiv preprint arXiv:2402.00399*, 2024.
- [34] T. D. Barfoot, C. H. Tong, and S. Särkkä, "Batch continuous-time trajectory estimation as exactly sparse gaussian process regression," in *Robotics: Science and Systems*, vol. 10. Citeseer, 2014, pp. 1–10.
- [35] S. Anderson and T. D. Barfoot, "Full steam ahead: Exactly sparse gaussian process regression for batch continuous-time trajectory estimation on se(3)," in *2015 IEEE Int. Conf. Intell. Rob. Syst.* IEEE, 2015, pp. 157–164.
- [36] F. M. Mirzaei and S. I. Roumeliotis, "A kalman filter-based algorithm for imu-camera calibration: Observability analysis and performance evaluation," *IEEE Trans. Rob.*, vol. 24, no. 5, pp. 1143–1156, 2008.
- [37] J. Nikolic, M. Burri, I. Gilitschenski, J. Nieto, and R. Siegwart, "Non-parametric extrinsic and intrinsic calibration of visual-inertial sensor systems," *IEEE Sensors J.*, vol. 16, no. 13, pp. 5433–5443, 2016.
- [38] X. Xiao, Y. Zhang, H. Li, H. Wang, and B. Li, "Camera-imu extrinsic calibration quality monitoring for autonomous ground vehicles," *IEEE Robot. Autom.*, vol. 7, no. 2, pp. 4614–4621, 2022.

- [39] C. Le Gentil, T. Vidal-Calleja, and S. Huang, “3d lidar-imu calibration based on upsampled preintegrated measurements for motion distortion correction,” in *2018 Proc. IEEE Int. Conf. Rob. Autom.* IEEE, 2018, pp. 2149–2155.
- [40] W. Liu, Z. Li, R. Malekian, M. A. Sotelo, Z. Ma, and W. Li, “A novel multifeature based on-site calibration method for lidar-imu system,” *IEEE Trans. Ind. Electron.*, vol. 67, no. 11, pp. 9851–9861, 2019.
- [41] S. Li, L. Wang, J. Li, B. Tian, L. Chen, and G. Li, “3d lidar/imu calibration based on continuous-time trajectory estimation in structured environments,” *IEEE Access*, vol. 9, pp. 138 803–138 816, 2021.
- [42] W. Wu, J. Li, C. Chen, B. Yang, X. Zou, Y. Yang, Y. Xu, R. Zhong, and R. Chen, “Affi-calib: Robust lidar-imu extrinsic self-calibration based on adaptive frame length lidar odometry,” *ISPRS J. Photogramm. Remote Sens.*, vol. 199, pp. 157–181, 2023.
- [43] J. Peršić, I. Marković, and I. Petrović, “Extrinsic 6dof calibration of 3d lidar and radar,” in *2017 European Conf. Mob. Robots, ECMR.* IEEE, 2017, pp. 1–6.
- [44] G. El Natour, O. A. Aider, R. Rouveure, F. Berry, and P. Faure, “Radar and vision sensors calibration for outdoor 3d reconstruction,” in *2015 Proc. IEEE Int. Conf. Rob. Autom.* IEEE, 2015, pp. 2084–2089.
- [45] E. Wise, J. Peršić, C. Grebe, I. Petrović, and J. Kelly, “A continuous-time approach for 3d radar-to-camera extrinsic calibration,” in *2021 Proc. IEEE Int. Conf. Rob. Autom.* IEEE, 2021, pp. 13 164–13 170.
- [46] C. Doer and G. F. Trommer, “Radar inertial odometry with online calibration,” in *2020 Eur. Navig. Conf., ENC.* IEEE, 2020, pp. 1–10.
- [47] J. Rehder, J. Nikolic, T. Schneider, T. Hinzmann, and R. Siegwart, “Extending kalibr: Calibrating the extrinsics of multiple imus and of individual axes,” in *2016 Proc. IEEE Int. Conf. Rob. Autom.* IEEE, 2016, pp. 4304–4311.
- [48] S. Li, X. Li, S. Chen, Y. Zhou, and S. Wang, “Targetless spatiotemporal calibration of multi-lidar multi-imu system based on continuous-time optimization,” *IEEE Trans. Ind. Inf.*, 2024.
- [49] J. Hartzer and S. Saripalli, “Online multi-imu calibration using visual-inertial odometry,” in *2023 IEEE Int. Conf. Multisensor Fusion Integr. Intell. Syst.* IEEE, 2023, pp. 1–7.
- [50] J. Lee, D. Hanley, and T. Bretl, “Extrinsic calibration of multiple inertial sensors from arbitrary trajectories,” *IEEE Robot. Autom.*, vol. 7, no. 2, pp. 2055–2062, 2022.
- [51] D. Tedaldi, A. Pretto, and E. Menegatti, “A robust and easy to implement method for imu calibration without external equipments,” in *2014 Proc. IEEE Int. Conf. Rob. Autom.* IEEE, 2014, pp. 3042–3049.
- [52] O. W. Holmes, “The stereoscope and the stereograph,” *Atlantic Monthly*, vol. 3, no. 1, 1859.
- [53] C. B. Duane, “Close-range camera calibration,” *Photogramm. Eng.*, vol. 37, no. 8, pp. 855–866, 1971.
- [54] J. Kannala and S. S. Brandt, “A generic camera model and calibration method for conventional, wide-angle, and fish-eye lenses,” *IEEE Trans. Pattern Anal. Mach. Intell.*, vol. 28, no. 8, pp. 1335–1340, 2006.
- [55] P. Biber and W. Straßer, “The normal distributions transform: A new approach to laser scan matching,” in *2003 IEEE Int. Conf. Intell. Rob. Syst.*, vol. 3. IEEE, 2003, pp. 2743–2748.
- [56] B. D. Lucas and T. Kanade, “An iterative image registration technique with an application to stereo vision,” in *IJCAI’81: 7th international joint conference on Artificial intelligence*, vol. 2, 1981, pp. 674–679.
- [57] L. Kneip and S. Lynen, “Direct optimization of frame-to-frame rotation,” in *Proc. IEEE Int. Conf. Comput. Vision*, 2013, pp. 2352–2359.
- [58] D. G. Lowe, “Distinctive image features from scale-invariant keypoints,” *Int. J. Comput. Vision*, vol. 60, pp. 91–110, 2004.
- [59] J. L. Schönberger and J.-M. Frahm, “Structure-from-motion revisited,” in *Proc IEEE Comput. Soc. Conf. Comput. Vision Pattern Recognit.*, 2016.
- [60] D. Duberg and P. Jensfelt, “Ufomap: An efficient probabilistic 3d mapping framework that embraces the unknown,” *IEEE Robot. Autom.*, vol. 5, no. 4, pp. 6411–6418, 2020.
- [61] S. Agarwal, K. Mierle, and T. C. S. Team, “Ceres Solver,” 10 2023. [Online]. Available: <https://github.com/ceres-solver/ceres-solver>
- [62] D. Schubert, N. Demmel, L. Von Stumberg, V. Usenko, and D. Cremers, “Rolling-shutter modelling for direct visual-inertial odometry,” in *2019 IEEE Int. Conf. Intell. Rob. Syst.* IEEE, 2019, pp. 2462–2469.
- [63] S. Chen, X. Li, S. Li, Y. Zhou, and S. Wang, “River: A tightly-coupled radar-inertial velocity estimator based on continuous-time optimization,” *IEEE Robot. Autom.*, 2024.
- [64] E. Süli and D. F. Mayers, *An introduction to numerical analysis*. Cambridge university press, 2003.



Shuolong Chen received the B.S. degree in geodesy and geomatics engineering from Wuhan University, Wuhan China, in 2023.

He is currently a master candidate at the School of Geodesy and Geomatics (SGG), Wuhan University. His area of research currently focuses on integrated navigation systems and multi-sensor fusion, mainly on spatiotemporal calibration.

Contact him via e-mail: shlchen@whu.edu.cn



Xingxing Li received the B.S. degree from Wuhan University, Wuhan China, in 2008, and the Ph.D. degree from the Department of Geodesy and Remote Sensing, German Research Centre for Geosciences (GFZ), Potsdam, Germany, in 2015.

He is currently a professor at the Wuhan University. His current research mainly involves GNSS precise data processing and multi-sensor fusion.

Contact him via e-mail: xxli@sgg.whu.edu.cn



Shengyu Li received the M.S. degree in geodesy and survey engineering from Wuhan University, Wuhan, China, in 2022.

He is currently a doctor candidate at the School of Geodesy and Geomatics (SGG), Wuhan University, China. His current research focuses on multi-sensor fusion and integrated navigation system.

Contact him via e-mail: lishengyu@whu.edu.cn



Yuxuan Zhou received the M.S. degree in geodesy and survey engineering from Wuhan University, Wuhan, China, in 2022.

He is currently a doctor candidate at the School of Geodesy and Geomatics (SGG), Wuhan University, China. His current research areas include integrated navigation systems, simultaneous localization and mapping, and multi-sensor fusion.

Contact him via e-mail: yuxuanzhou@whu.edu.cn



Xiaoteng Yang received the B.S. degree in geodesy and geomatics engineering from Wuhan University, Wuhan China, in 2023.

He is currently a master candidate at the School of Geodesy and Geomatics (SGG), Wuhan University, also a member of the Mobile Autonomous Sensing And Surveying LAB. His current research mainly involves UAV-based multi-sensor fusion and integrated navigation system.

Contact him via e-mail: xyang@whu.edu.cn